ELSEVIER

Journal of Fluids and Structures 21 (2005) 743–767

JOURNAL OF FLUIDS AND STRUCTURES

www.elsevier.com/locate/jfs

Influence of boundary conditions relaxation on panel flutter with compressive in-plane loads

D.M. Beloiu[a], R.A. Ibrahim[a,*], C.L. Pettit[b]

[a]*Wayne State University, Department of Mechanical Engineering, Detroit, MI 48202, USA*
[b]*Air Force Research Laboratory, AFRL/VASD, Wright-Patterson Air Force Base, OH 45433, USA*

Received 1 September 2004; accepted 20 July 2005
Available online 18 October 2005

Abstract

The influence of boundary conditions relaxation on two-dimensional panel flutter is studied in the presence of in-plane loading. The boundary value problem of the panel involves time-dependent boundary conditions that are converted into autonomous form using a special coordinate transformation. Galerkin's method is used to discretize the panel partial differential equation of motion into six nonlinear ordinary differential equations. The influence of boundary conditions relaxation on the panel modal frequencies and LCO amplitudes in the time and frequency domains is examined using the windowed short time Fourier transform and wavelet transform. The relaxation and system nonlinearity are found to have opposite effects on the time evolution of the panel frequency. Depending on the system damping and dynamic pressure, the panel frequency can increase or decrease with time as the boundary conditions approach the state of simple supports. Bifurcation diagrams are generated by taking the relaxation parameter, dynamic pressure, and in-plane load as control parameters. The corresponding largest Lyapunov exponent is also determined. They reveal complex dynamic characteristics of the panel, including regions of periodic, quasi-periodic, and chaotic motions.

1. Introduction

It has been observed that apparently identical aircraft can exhibit different dynamic characteristics under the same flight conditions. This difference owes its origin to the stochastic nature of structural properties and the environment. That is, the sensitivity of the dynamic system behavior is directly linked to variations in its physical properties. The physical properties of aeroelastic structures are affected by boundary conditions relaxation and joint uncertainties. Generally, the main sources of uncertainties of aerospace structures include:

(i) randomness in material properties due to variations in material composition;
(ii) randomness in structural dimensions due to manufacturing variations and thermal effects;
(iii) randomness in boundary conditions due to preload and relaxation variations in mechanical joints;
(iv) randomness of external excitations.

*Corresponding author. Tel.: +1 313 577 3885; fax: +1 313 577 8789.
E-mail address: raouf_ibrahim@eng.wayne.edu (R.A. Ibrahim).

0889-9746/$ - see front matter © 2005 Elsevier Ltd. All rights reserved.
doi:10.1016/j.jfluidstructs.2005.07.007

The present work deals with the third source and its mechanisms. There are many factors that affect mechanical joints and fasteners, such as friction, hardness, finish, and dimensions of all parts, and gasket creep (Bickford, 1990). Each factor will vary from fastener to fastener and joint to joint because of manufacturing or usage tolerances. A fastener subjected to vibration will not lose all pre-loads immediately. First there is a slow loss of pre-load caused by various relaxation mechanisms. Vibration increases relaxation through consequent wear and hammering. After sufficient pre-load is lost, friction forces drop below a critical level and, if the joint is bolted, the nut actually starts to back off and shake loose. As relaxation occurs, the joint fails to mimic ideal boundary conditions; instead, the joint's properties become time dependent and uncertain.

The present work is motivated by some recent results on the sensitivity and variability of the response of structural stochasticity [see, for example, Ibrahim (1987) and Manohar and Ibrahim (1999)] and by the recent assessment of joint uncertainties by Ibrahim and Pettit (2004). These problems are complex in nature because every joint involves different sources of uncertainty and nonsmooth nonlinear characteristics. For example, the contact forces are not ideally plane because of manufacturing tolerances. Furthermore, the initial forces will be redistributed nonuniformly in the presence of lateral loads. This is in addition to the prying load, which induces nonlinear tension in the bolt and nonlinear compression in the joint. The main problems encountered in the design analysis of bolted joints with parameter uncertainties include random eigenvalues, response statistics, and probability of failure.

The effect of uncertainty in the boundary conditions combined with the variability of material properties on the nonlinear panel aeroelastic response was studied by Lindsley et al. (2002a, b). It was shown that the flutter problem of aeroelastic structures could be handled when random uncertainties are introduced in the structural model. The pinned and fixed boundary conditions were modelled as limiting cases of rotational springs on the boundary, which possess zero and infinite stiffness, respectively. Accordingly, rotational spring stiffness was used to parameterize the boundary conditions. Parametric uncertainty was examined by modelling variability in Young's modulus and the boundary condition parameter. The variability in the boundary conditions was restricted to a single value along the plate boundary edges for each realization. For values of the dynamic pressure in the deterministic limit cycle oscillation (LCO) range, the variability in the boundary conditions affects the plate deflection in an essentially linear manner. However, for values of dynamic pressure in the neighborhood of the bifurcation point, the relationship is nonlinear. Variation in boundary conditions results in a softening effect of the clamped panel, and thus induces an increase in the amplitude of plate oscillations.

Structural and material uncertainties were also considered in studying the flutter of panels and shells by Liaw and Yang (1991a, b) and Kuttenkeuler and Ringertz (1998). For example, Liaw and Yang (1991a, b) quantified the effect of parameter uncertainties on the reduction of the structural reliability and stability boundaries of initially compressed laminated plates and shells. For buckling analysis, the uncertainties include modulus of elasticity, thickness, and fiber orientation of individual lamina, as well as geometric imperfections. For flutter analysis, further uncertainties such as mass density, air density, and in-plane load were also considered. Kuttenkeuler and Ringertz (1998) performed an optimization study of the onset of flutter, with respect to material and structural uncertainties, both experimentally and numerically, using finite element analysis and the doublet-lattice method.

A ground vibration test was used by Potter and Lind (2001) to obtain uncertainty models, such as natural frequencies and their associated variations, which can update analytical models for the purpose of predicting robust flutter speeds. Different norm approaches were used to formulate uncertainty models that cover the entire range of observed variations. It was found that the ∞-norm produces the smallest uncertainty and the least conservative robust flutter speed. Lind and Brenner (2000) introduced a tool referred to as the "flutterometer" for predicting the onset of flutter during a flight test. The flutterometer computes a flutter for an analytical model with respect to an uncertainty description. Brenner (2002a) considered a technique that identifies model parameters and their associated variances from flight data. Later Prazenica et al. (2003) introduced a technique for estimating uncertainty descriptions based on a wavelet approach, but relies on the Volterra kernels.

The studies of panel flutter were concentrated on parametric analysis of stability boundaries and the amplitude of LCO under different boundary conditions. At the same time, it was shown that a panel subjected to a combination of airflow and in-plane loading experiences a complex range of motions, including static buckling (divergence), quasi-periodic motion, and chaos in addition to LCO. Dowell (1982) showed that a panel under the combined effect of fluid flow and in-plane compression exhibits chaotic motion for certain values of some control parameters. Dowell (1984) observed chaos, via period doubling and intermittency while increasing the compressive in-plane loading. The existence of multiple attractors and the coexistence of both symmetric and asymmetric LCO were observed by Bolotin et al. (1998) using a two degree-of-freedom approximation of an elastic panel. They studied the transition between different stability regions. The stability regions of a simply supported two-dimensional panel subjected to compressive loading were revisited recently by Epureanu et al. (2004). They used bifurcation diagrams for two control parameters to determine stability boundaries and Lyapunov exponents. The effect of damping on stability boundaries as well as on

LCO was considered by Kuo et al. (1972), Bismarck-Nasr and Bones (2000), Bolotin et al. (2002), Pourtakdoust and Fazelzadeh (2003). Kuo et al. (1972) showed that the edge compression and viscous structural damping would result in an increase of flutter amplitudes while the aerodynamic damping would cause a reduction in the flutter amplitude.

Relaxation effects cause time-dependent boundary conditions and depend on the level of structural vibration. In other words, there are uncertainties in the boundary conditions in addition to a random field due to system parameter uncertainties. In this case, aeroelastic structures will experience nonstationary time–frequency flutter, which is analyzed using time–frequency transforms such as spectrographs and wavelet transform. The time–frequency analysis techniques have recently been used to analyze flight flutter data by Brenner (1997), Johnson et al. (2002), Staszewski and Cooper (2002), and Yu et al. (2004). Brenner (1997) used time–frequency signal representations to analyze aeroelastic flight data. Mastroddi and Bettoli (1999) conducted wavelet analysis in the neighborhood of a Hopf bifurcation to capture the features of transient responses. In the neighborhood of aeroelastic flutter during flight tests, the time scale decompositions of continuous wavelet transform was used to analyze pre- and post-critical transient behavior of nonlinear aeroelastic structures. Brenner (2002b) applied the singular-value decomposition to aeroelastic pitch-plunge wing section models to detect instability and nonlinear dynamics from the time-frequency map.

The present work deals with the nonlinear panel flutter with relaxation in boundary conditions. The conventional boundary value problem of the panel involves time-dependent boundary conditions, which are converted to an autonomous form using a special coordinate transformation inspired by the work of Qiao et al. (2000). The present analysis extends the analysis of Ibrahim et al. (2004) to include six-mode interaction in the presence of boundary condition relaxation. The dynamic characteristics of the panel and the influence of initial conditions are predicted using phase plots, FFT plots, bifurcation diagrams of the first return, short time Fourier transform, wavelet transform, and Lyapunov exponent.

2. Analytical modelling

Consider a two-dimensional panel exposed to supersonic flow as shown in Fig. 1. In order to estimate the work done by aerodynamic loading, the pressure on the panel is represented by the linear piston theory (Ashley and Zartarian, 1956),

$$\Delta p = p - p_\infty = \frac{\rho_\infty U_\infty^2}{M}\left[\frac{\partial w}{\partial x} + \frac{1}{U_\infty}\frac{\partial w}{\partial t}\right], \tag{1}$$

where $w(x,t)$ is the panel deflection, which is a function of position, x, and time, t. $M = U_\infty/a_\infty$ is the Mach number, U_∞ is the undisturbed gas flow speed, $a_\infty = \sqrt{\gamma p_\infty/\rho_\infty}$ is the speed of sound, p_∞ and ρ_∞ are the undisturbed free gas stream pressure and density, respectively. p is the pressure of the gas flow at the panel surface, $\gamma = C_p/C_v$ is the ratio of specific heats at constant pressure, C_p, and volume, C_v.

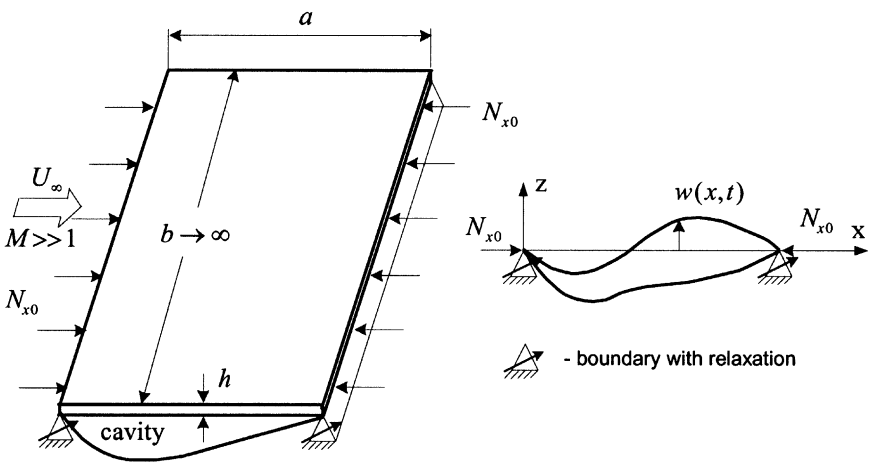

Fig. 1. Schematic diagram of a two-dimensional panel with boundary conditions relaxation.

The governing nonlinear equation of motion for the panel is developed using Hamilton's principle, which yields (Ibrahim et al., 1990)

$$m_p\frac{\partial^2 w}{\partial t^2}+D\left(1+c\frac{\partial}{\partial t}\right)\frac{\partial^4 w}{\partial x^4}-\left[N_{x0}+\frac{Eh}{2a}\int_0^a\left(\frac{\partial w}{\partial x}\right)^2\mathrm{d}x\right]\frac{\partial^2 w}{\partial x^2}+\frac{\rho_\infty U_\infty^2}{M}\left[\frac{\partial w}{\partial x}+\frac{1}{U_\infty}\frac{\partial w}{\partial t}\right]=\Delta p_0, \tag{2}$$

where m_p is the panel mass per unit area, a is the panel length, E is Young's modulus, h is the plate thickness, $D=Eh^3/[12(1-\nu^2)]$ is the panel stiffness, ν is Poisson's ratio, Δp_0 is the gas pressure difference across the panel, N_{x0} is the external in-plane load per unit span-wise length, and c is a linear viscous damping coefficient. Eq. (2) is subject to the boundary conditions

$$D\frac{\partial^2 w(0,t)}{\partial x^2}-\alpha_1(t)\frac{\partial w(0,t)}{\partial x}=0,\quad w(0,t)=0, \tag{3a,b}$$

$$D\frac{\partial^2 w(a,t)}{\partial x^2}+\alpha_2(t)\frac{\partial w(a,t)}{\partial x}=0,\quad w(a,t)=0, \tag{3c,d}$$

where $\alpha_1(t)$ and $\alpha_2(t)$ measure the end slopes and represent torsional stiffness parameters such that if $\alpha_1(t)=\alpha_2(t)=\infty$ the panel is purely clamped–clamped. On the other hand, the panel is simply supported if $\alpha_1(t)=\alpha_2(t)=0$. In real situations, $\alpha_1(t)$ and $\alpha_2(t)$ do not assume these limiting cases; instead, they are very large for clamped supports or very small for simple supports. In the dynamic case the boundary conditions (3a,c) are nonautonomous. In order to convert these conditions into an autonomous form, we introduce the following transformation of the response coordinate:

$$w(x,t)=\left[\left(\frac{x}{a}\right)^2+2g_1(z_1,z_2)\frac{x}{a}+g_2(z_1,z_2)\right]u(x,t)=\varphi(x;z_1,z_2)u(x,t), \tag{4}$$

where the dimensionless parameter $z_i(t)=D/a\alpha_i(t)$, $i=1,2$, represents the ratio of the bending rigidity to the torsional stiffness of the joints. One may also adopt other alternative of using the original boundary conditions (3) in a Rayleigh–Ritz formulation of $w(x,t)$ in terms of sine modes. In transformation (4), the functions $g_1(z_1,z_2)$ and $g_2(z_1,z_2)$ are chosen to render the boundary conditions autonomous for the new coordinate $u(x,t)$. Possible expressions of these functions are

$$g_1(z_1,z_2)=-\frac{1+4z_2}{2(1+2z_1+2z_2)},\quad g_2(z_1,z_2)=-\frac{2z_1(1+4z_2)}{1+2z_1+2z_2}. \tag{5}$$

In this case, boundary conditions (3) become

$$\frac{\partial^2 u(0,t)}{\partial x^2}=\frac{\partial^2 u(a,t)}{\partial x^2}=0\quad\text{and}\quad u(0,t)=u(a,t)=0. \tag{6}$$

Introducing the following nondimensional parameters

$$\tau=t\sqrt{\frac{D}{m_p a^4}},\quad \bar{w}=\frac{w}{h},\quad \bar{x}=\frac{x}{a},\quad \lambda=\frac{\rho_\infty U_\infty^2 a^3}{MD},\quad \mu=\frac{\rho_\infty a}{m_p},\quad \zeta=\frac{c}{a^2}\sqrt{\frac{D}{m_p}},\quad \bar{N}_0=N_{x0}\frac{a^2}{D},\quad \bar{u}=\frac{u}{h},$$

$$\bar{p}_0=\Delta p_0\frac{a^4}{Dh},\quad B_1=6(1-\nu^2),\quad \bar{\varphi}=\left[\bar{x}^2+2g_1(z_1,z_2)\bar{x}+g_2(z_1,z_2)\right],\quad \hat{\zeta}=\sqrt{\frac{\mu}{M}},$$

Eq. (2) becomes

$$\frac{\partial^2(\bar{\varphi}\bar{u})}{\partial\tau^2}+\left(1+\zeta\frac{\partial}{\partial\tau}\right)\frac{\partial^4(\bar{\varphi}\bar{u})}{\partial\bar{x}^4}-\left[\bar{N}_0+B_1\int_0^1\left(\frac{\partial(\bar{\varphi}\bar{u})}{\partial\bar{x}}\right)^2\mathrm{d}\bar{x}\right]\frac{\partial(\bar{\varphi}\bar{u})}{\partial\bar{x}^2}+\lambda\frac{\partial(\bar{\varphi}\bar{u})}{\partial\bar{x}}+\hat{\zeta}\sqrt{\lambda}\frac{\partial(\bar{\varphi}\bar{u})}{\partial\tau}=\bar{p}_0. \tag{7}$$

The relaxation process is phenomenologically modelled based on experimental results (Bickford, 1990). In this case, The torsional stiffness parameters are assumed functions of the number of vibration cycles, $n=n(\tau)$,

$$\bar{\alpha}_i(n)=\frac{a\alpha_i(n)}{D}=\frac{1}{z_i(n)}, \tag{8}$$

where the overbar denotes a dimensionless parameter. An explicit analytical expression for the parameters $\bar{\alpha}_i(n)$ can be obtained from experimental records (Bickford, 1990), which reveal a slow drop between an original and an asymptotic value of the joint stiffness. An appropriate elementary function that emulates this behavior may be

selected in the form

$$\bar{\alpha}(n) = \bar{\alpha}(\infty) + [\bar{\alpha}(0) - \bar{\alpha}(\infty)]\left[\frac{1 + \tanh[-k(n - n_c)]}{1 + \tanh[kn_c]}\right], \tag{9}$$

where the subscript i has been dropped, and n_c is a critical number of cycles, indicating the location of the inflection point with respect to the origin, $n = 0$. The parameter k is associated with the slope of the curve at the point, $n = n_c$. The parameters $\bar{\alpha}(0)$ and $\bar{\alpha}(\infty)$ are obtained from the experimental curve. The slope parameter k can be found by taking the derivative of Eq. (9) with respect to n, i.e.,

$$k = \frac{\partial\bar{\alpha}(n)/\partial n|_{n_c}}{[\bar{\alpha}(\infty) - \bar{\alpha}(0)]}[1 + \tanh[kn_c]]. \tag{10}$$

One can write an expression for $z(\tau)$ by using relations (8) and (10) in the form

$$z(\tau) = Z_0 Z_\infty \left[Z_0 - (Z_0 - Z_\infty)\frac{1 + \tanh(-\chi(\tau - \tau_c))}{1 + \tanh(\chi\tau_c)}\right]^{-1}, \tag{11}$$

where $Z_0 = z(0)$, $Z_\infty = z(\infty)$, $\chi = \langle\varpi\rangle/2\pi k$, and $\langle\varpi\rangle$ is the mean value of the response frequency, which can be taken as the center frequency. The phenomenological representation given by Eq. (11) can be used for any initial preload and will cause the panel to experience nonstationary behavior.

Galerkin's method is applied by substituting the general solution $\bar{u}(\bar{x},\tau) = \sum_{n=1}^{N}\Psi_n(\bar{x})q_n(\tau)$ into Eq. (7), where $q_n(\tau)$ are unknown functions to be determined (generalized coordinates), $\Psi_n(\bar{x})$ are the assumed orthonormal mode shapes, and N is the total number of the basis functions for $\bar{u}(\bar{x},\tau)$. Multiplying both sides by the corresponding weighting functions $\tilde{u}(\bar{x},\tau) = \sum_{n=1}^{N}\Psi_n(\bar{x})\tilde{q}_n(\tau)$, where $\tilde{q}_n(\tau)$ are arbitrary functions of time, and integrating both sides with respect to $\bar{x}$, the resulting discretized equations are obtained by setting the coefficients of each arbitrary function $\tilde{q}_n(\tau)$ to zero. The resulting ordinary differential equations may be written in the form

$$\begin{aligned}
&\sum_{n=1}^{N}\ddot{q}_n(\tau)\Delta_{nm} + \sum_{n=1}^{N}q_n(\tau)C_1(n,m) + \zeta\sum_{n=1}^{N}\dot{q}_n(\tau)C_1(n,m) - \sum_{n=1}^{N}q_n(\tau)\bar{N}_{x0}C_2(n,m)\\
&\quad - B_1\sum_{n=1}^{N}q_n(\tau)C_2(n,m)\left(\int_0^1\left(\sum_{n=1}^{N}q_k(\tau)(\varphi'(\bar{x})\Psi_k(\bar{x}) + \varphi(\bar{x})\Psi_k'(\bar{x}))\right)^2\mathrm{d}\bar{x}\right)\\
&\quad + \lambda\sum_{n=1}^{N}q_n(\tau)[D_1(n,m) + D_2(n,m)] + \hat{\zeta}\sqrt{\lambda}\sum_{n=1}^{N}\dot{q}_n(\tau)\Delta_{nm} = \bar{p}_0 D_4(m),
\end{aligned} \tag{12}$$

where a dot denotes differentiation with respect to the nondimensional time parameter τ, a prime denotes differentiation with respect to the nondimensional spatial coordinate $\bar{x}$,

$$\Delta_{nm} = \int_0^1\varphi(\bar{x})\Psi_n(\bar{x})\Psi_m(\bar{x})\mathrm{d}\bar{x},$$

$$\begin{aligned}
C_1(n,m) &= 6\int_0^1\varphi''(\bar{x})\Psi_n''(\bar{x})\Psi_m(\bar{x})\,\mathrm{d}\bar{x} + 4\int_0^1\varphi^{(3)}(\bar{x})\Psi_n'(\bar{x})\Psi_m(\bar{x})\,\mathrm{d}\bar{x}\\
&\quad + 4\int_0^1\varphi'(\bar{x})\Psi_n^{(3)}(\bar{x})\Psi_m(\bar{x})\,\mathrm{d}\bar{x} + \int_0^1\varphi^{(4)}(\bar{x})\Psi_n(\bar{x})\Psi_m(\bar{x})\,\mathrm{d}\bar{x} + \int_0^1\varphi(\bar{x})\Psi_n^{(4)}(\bar{x})\Psi_m(\bar{x})\,\mathrm{d}\bar{x},
\end{aligned}$$

$$C_2(n,m) = 6\int_0^1\varphi''(\bar{x})\Psi_n(\bar{x})\Psi_m(\bar{x})\,\mathrm{d}\bar{x} + 2\int_0^1\varphi'(\bar{x})\Psi_n'(\bar{x})\Psi_m(\bar{x})\,\mathrm{d}\bar{x} + 6\int_0^1\varphi(\bar{x})\Psi_n''(\bar{x})\Psi_m(\bar{x})\,\mathrm{d}\bar{x},$$

$$D_1(n,m) = \int_0^1\varphi'(\bar{x})\Psi_n(\bar{x})\Psi_m(\bar{x})\,\mathrm{d}\bar{x}; \quad D_2(n,m) = \int_0^1\varphi(\bar{x})\Psi_n'(\bar{x})\Psi_m(\bar{x})\,\mathrm{d}\bar{x}$$

$$D_4(m) = \int_0^1\Psi_m(\bar{x})\,\mathrm{d}\bar{x}.$$

The general solution is assumed in the form

$$\bar{u}(\bar{x},\tau) = \sum_{n=1}^{N}q_n(\tau)\sin n\pi\bar{x}, \tag{13}$$

where N is the total number of modes, $q_n(\tau)$ are the generalized coordinates. It has been established that accurate solution of the panel flutter can be achieved by using at least six modes [see, e.g., Dowell (1966)]. The inclusion of six modes results in more tedious analysis and for this reason we introduce the simplification, $z_1 = z_2 = z/2$, which makes the boundary stiffness values to be equal, and gives $g_1 = -1/2$ and $g_2 = -z$. The resulting set of six equations may be written in matrix form

$$[\mathbf{M}(\tau)]\{\ddot{\mathbf{q}}\} + [\mathbf{C}(\zeta, \hat{\zeta}, \lambda, \tau)]\{\dot{\mathbf{q}}\} + [\mathbf{K}(\tau, \bar{\mathbf{N}}_0, \lambda)]\{\mathbf{q}\} = [\mathbf{D}(\tau)]\{\mathbf{q}^3\} + \sum_{i=1,3,5} \sum_{j=1, j\neq i}^{6} \{\boldsymbol{e}(\tau)\mathbf{q}_i\mathbf{q}_j^2\} + \sum_{i} \sum_{j}^{i\neq j\neq k} \sum_{k} \{\mathbf{f}(\tau)\mathbf{q}_i\mathbf{q}_j\mathbf{q}_k\} + \{\mathbf{P}(\tau)\}, \tag{14}$$

where $[\boldsymbol{M}(\tau)]$ is time–dependent mass matrix, $[\boldsymbol{C}(\zeta, \hat{\zeta}, \lambda, \tau)]$ is the damping matrix, which depends on the viscous damping ratio ζ, mass parameter, $\hat{\zeta}$, and relaxation parameter, $z(\tau)$. $[\boldsymbol{K}(\tau, \bar{N}_0, \lambda)]$ is the stiffness matrix, $[\boldsymbol{D}(\tau)]$ is the coefficient matrix of cubic terms, and $\{\boldsymbol{P}(\tau)\}$ is the pressure vector, whose elements are nonzero only for odd modes. The structure of these matrices is given in the appendix. The complete set of expressions for all coefficients of the matrices and vectors of Eq. (14) is documented in Beloiu (2005).

Eqs. (14) are solved numerically in the time domain for a typical relaxation curve. The resulting solution is given in terms of the transformed response, $\bar{u}$, or rather in terms of its modal coordinates, q_i, $i = 1, \ldots, 6$. One should estimate the modal response in terms of its physical generalized coordinate,

$$\bar{w}(\bar{x}, \tau) = \sum_{n=1}^{N} \hat{q}_n(\tau) \sin n\pi\bar{x} = \bar{\varphi}(\bar{x})\bar{u}(\bar{x}, \tau), \tag{15}$$

where $\bar{\varphi} = [\bar{x}^2 + 2g_1(z_1, z_2)\bar{x} + g_2(z_1, z_2)]$ and g_i are given by Eq. (5). The relationship between the physical coordinates $\hat{q}_n(\tau)$ and the generalized transformed coordinates $q_n(\tau)$ is

$$\bar{w}(\bar{x}, \tau) = \sum_{n=1}^{N} \hat{q}_n(\tau) \sin\, n\pi\bar{x} = \left[\bar{x}^2 + 2g_1(z)\bar{x} + g_2(z)\right] \sum_{n=1}^{N} q_n(\tau) \sin\, n\pi\bar{x}. \tag{16}$$

Multiplying both sides of Eq. (16) by $\sin\, m\pi\bar{x}$, $m = 1, 2, \ldots, 6$, and integrating both sides

$$\int_0^1 \left[\sum_{n=1}^{N} \hat{q}_n(\tau)\, \sin\, n\pi\bar{x}\, \sin\, m\pi\bar{x}\right] \mathrm{d}\bar{x} = \int_0^1 \left[(\bar{x}^2 + 2g_1(z)\bar{x} + g_2(z)) \sum_{n=1}^{N} q_n(\tau) \sin\, n\pi\bar{x}\, \sin\, m\pi\bar{x}\right] \mathrm{d}\bar{x}$$

gives the desired relation between the coordinates:

$$\begin{Bmatrix} \hat{q}_1 \\ \hat{q}_3 \\ \hat{q}_5 \end{Bmatrix} = \begin{bmatrix} T_{11} & T_{13} & T_{15} \\ T_{31} & T_{33} & T_{35} \\ T_{51} & T_{53} & T_{55} \end{bmatrix} \begin{Bmatrix} q_1 \\ q_3 \\ q_5 \end{Bmatrix} \quad \text{and} \quad \begin{Bmatrix} \hat{q}_2 \\ \hat{q}_4 \\ \hat{q}_6 \end{Bmatrix} = \begin{bmatrix} T_{22} & T_{24} & T_{26} \\ T_{42} & T_{44} & T_{46} \\ T_{62} & T_{64} & T_{66} \end{bmatrix} \begin{Bmatrix} q_2 \\ q_4 \\ q_6 \end{Bmatrix}, \tag{17}$$

where

$$\begin{aligned} &T_{11} = -\frac{3 + \pi^2(1 + 6z)}{6\pi^2}, \quad T_{22} = -\frac{3 + 4\pi^2(1 + 6z)}{24\pi^2}, \quad T_{33} = -\frac{1 + 3\pi^2(1 + 6z)}{18\pi^2}, \\ &T_{44} = -\frac{3 + 16\pi^2(1 + 6z)}{96\pi^2}, \quad T_{55} = -\frac{3 + 25\pi^2(1 + 6z)}{150\pi^2}, \quad T_{66} = -\frac{1 + 12\pi^2(1 + 6z)}{72\pi^2}, \\ &T_{13} = T_{31} = \frac{3}{8\pi^2}, \quad T_{15} = T_{51} = \frac{5}{72\pi^2}, \quad T_{24} = T_{42} = \frac{4}{9\pi^2}, \\ &T_{26} = T_{62} = \frac{3}{32\pi^2}, \quad T_{35} = T_{53} = \frac{15}{32\pi^2}, \quad T_{46} = T_{64} = \frac{12}{25\pi^2}. \end{aligned} \tag{18}$$

The next section presents the stability analysis and response characteristics under different values of dynamic pressure and relaxation parameter.

3. Linear analysis

The stability analysis is carried out by estimating the natural frequencies of the six modes in the absence of system nonlinearities and by setting the nonhomogeneous term in Eqs. (14) to zero. The dependence of the real and imaginary components of the eigenvalues on the dynamic pressure in shown in Figs. 2(a) and (b) for three different values of the relaxation parameter ($z = 0.001$, 0.1, and 1), damping parameter, $\zeta = 0.0$, mass parameter $\hat{\zeta} = 0.1$, and static axial load parameter $\bar{N}_0 = 0$. It is seen that the real parts are zero up to a critical value of the dynamic pressure, depending on the value of the relaxation parameter, z, above which one becomes negative and the other positive indicating the occurrence of panel instability (flutter). Note that the value $z = 0.0$ corresponds to a clamped–clamped panel, while $z = \infty$ corresponds to simple supports. The dependence of the components of the first and second eigenvalues on the relaxation parameter, z, is shown in Fig. 3 for three different values of dynamic pressure, $\lambda = 400$, 450, and 500. It has seen that the eigenvalues posses negative real parts up to a critical value of relaxation parameter, above which one eigenvalue has a positive real part indicating the occurrence of flutter.

Figs. 4 and 5 show the boundaries of panel further in terms of the critical value of aerodynamic pressure, λ_{cr}, and the relaxation parameter, z. These figures depict the influence of the in-plane load, $\bar{N}_0$, and damping ratio, ζ, respectively. As expected, the compression in-plane loading results in a reduction of the critical flutter speed. The clamped panel ($z \ll 1$) requires more in-plane compression load to reach in flutter speed. With reference to Fig. 5, for all values of relaxation parameter, the damping is nonbeneficial as it increases from very small values up to a critical value, above which it becomes beneficial, depending on the value of the relaxation parameter. Fig. 6 shows the dependence of flutter speed on the damping parameter, ζ. For a given relaxation parameter, there is a critical damping ratio, ζ_{cr}, above which the damping becomes beneficial and the critical speed increases with the damping. The value of ζ_{cr} is shown by a small circle on each curve and is determined by setting $d\lambda/d\zeta = 0$. The locus of these points is shown by the dash–dotted

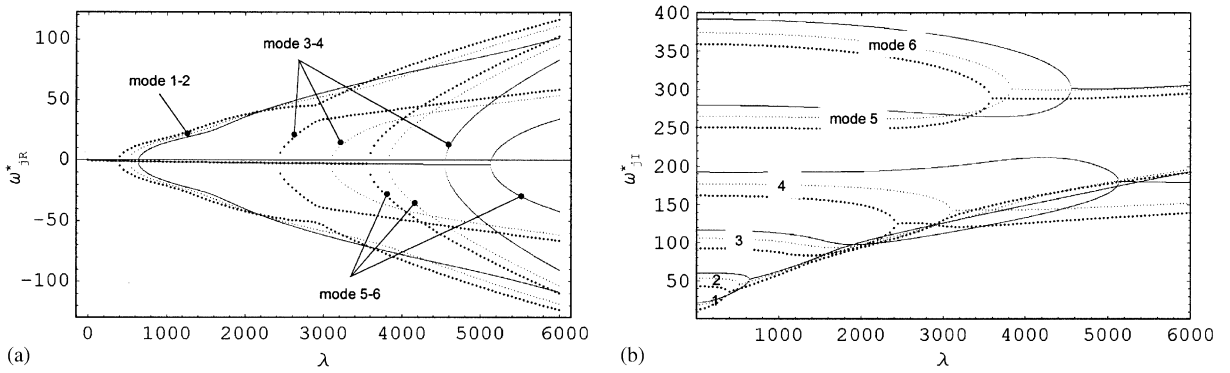

Fig. 2. Dependence of real and imaginary parts of the panel natural frequency on dynamic pressure for $\zeta = 0$, $\hat{\zeta} = 0.1$, $\bar{N}_0 = 0$: (a) real parts; (b) imaginary parts. —, $z = 0.001$; ……, $z = 0.1$; •••••, $z = 1$.

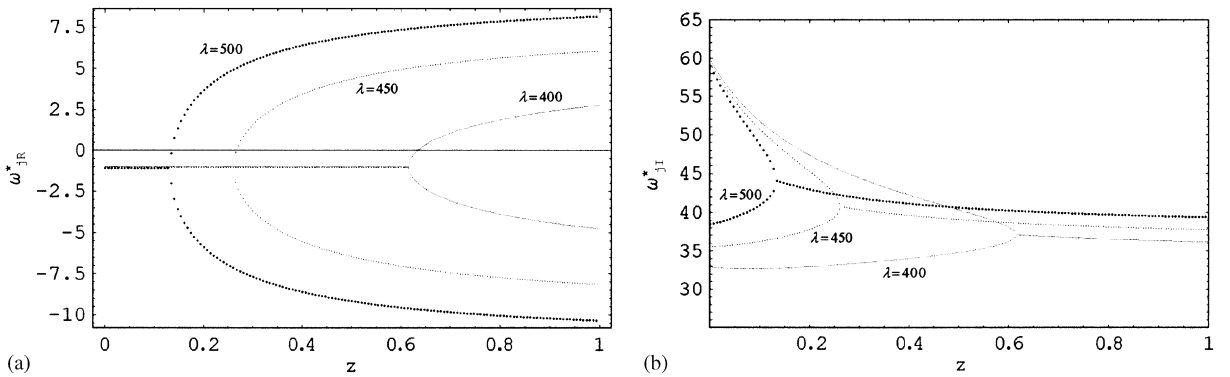

Fig. 3. Dependence of real and imaginary parts of the first and second natural frequencies on relaxation parameter z for $\zeta = 0$, $\hat{\zeta} = 0.1$, $\bar{N}_0 = 0$: (a) real parts; (b) imaginary parts. —, $\lambda = 400$, …, $\lambda = 450$, •••, $\lambda = 500$.

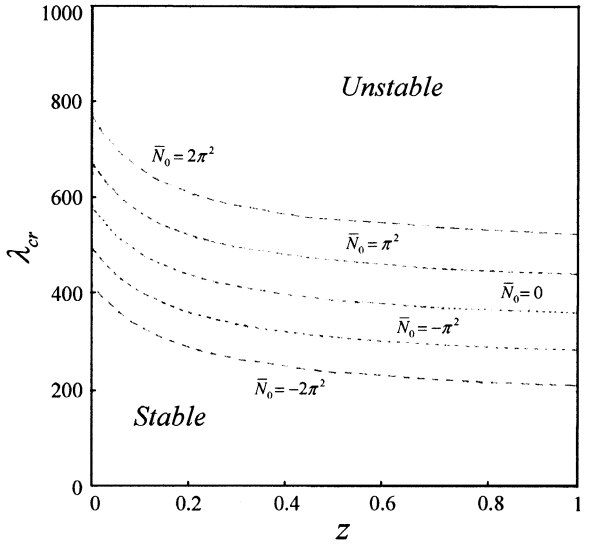

Fig. 4. Boundaries of panel flutter on the plane for different values of in-plane load and for $\hat{\zeta} = 0.1$, $\zeta = 0.0001$.

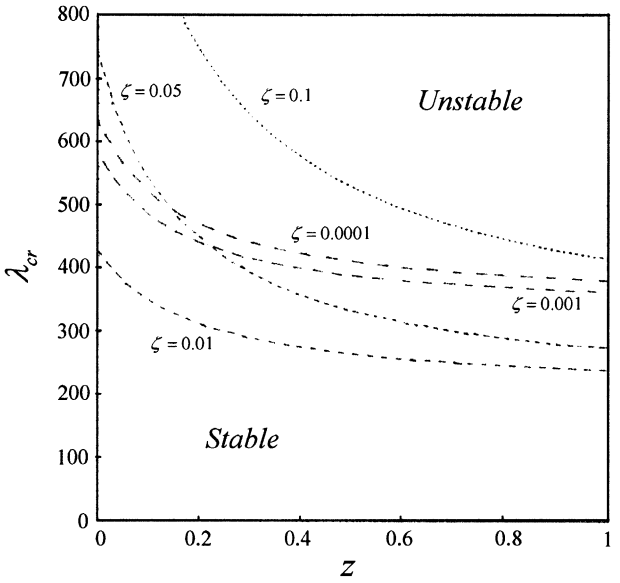

Fig. 5. Boundaries of panel flutter for different values of damping factor showing the reversal effect of damping for $\hat{\zeta} = 0.1$, $\bar{N}_0 = 0$.

curve. This curve separates two regions such that $\zeta < \zeta_{cr}$ the damping is detrimental and results in a reduction of the flutter speed, i.e., λ_{cr} decreases with damping until damping reaches the critical value ζ_{cr}. As $\zeta > \zeta_{cr}$ the damping results in a monotonic increase of λ_{cr}.

4. Nonlinear analysis

4.1. Bifurcation analysis

The complete set of Eqs. (14) is solved numerically using the MATLAB© variable solver ode15 with relative error tolerance of 10^{-6} and absolute error tolerance of 10^{-9}. The numerical solution is carried out for a given damping

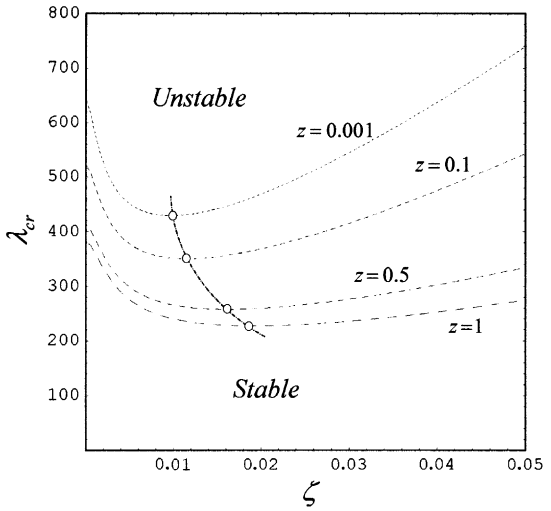

Fig. 6. Boundaries of panel flutter on the $\lambda-\zeta$ plane for different values of relaxation parameter, z, and for $\bar{N}_0 = 0.0$; $\hat{\zeta} = 0.1$. Dashed curve indicates the critical damping ratio that separate between stabilizing and destabilizing damping effects.

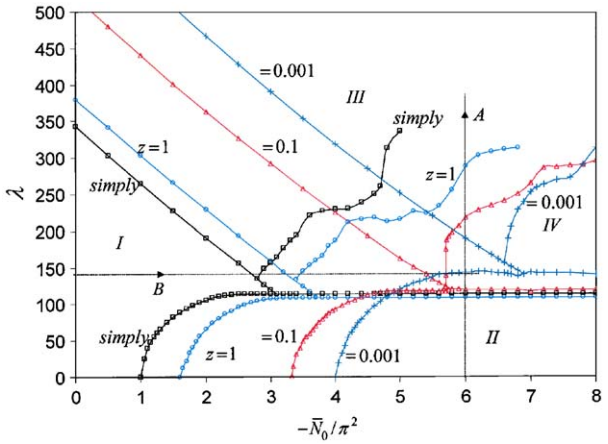

Fig. 7. Bifurcation diagram showing the regions of different panel regimes for damping parameter $\zeta = 0.0001$ and different values of relaxation parameter. (I) Statically stable, (II) static buckling (divergence), (III) LCO, and (IV) multi-period oscillations and chaos.

parameter, ζ, and for different values of in-plane load, $\bar{N}_0$, dynamic pressure, λ, and relaxation parameter, z. In order to avoid the influence of transient motion, only the last portion of the steady–state time history is taken to estimate the state of the panel. Depending on the system parameters and dynamic pressure the panel may exhibit different regimes such as (I) statically stable, (II) static buckling (divergence), (III) limit cycle oscillations, and (IV) multi-period oscillations and chaos. Fig. 7 shows these four regimes on the plane of dynamic pressure, λ, versus in-plane load, $-\bar{N}_0/\pi$, for three different values of relaxation parameter $z = 0.001$, 0.1, and 1, in addition to the case of simply supported panel. The two values of in-plane loads $-\bar{N}_0/\pi = 1$ and 4 represent the Euler buckling loads of simply supported and clamped panels, respectively. It is seen that as the relaxation parameter increases (panel approaches simply supported case) the regions (III) of LCO and (IV) multi-period oscillations/chaos expand. The dynamics of the panels along lines A and B shown in Fig. 7 will be examined later.

Fig. 8 shows the dependence of LCO amplitude on dynamic pressure for zero in-plane loading and different discrete values of the relaxation parameter z. Note that, depending on the value of the relaxation parameter, there is a critical value of dynamic pressure at which LCO begins in the form of supercritical bifurcation. The relaxation results in moving the bifurcation point to lower values of dynamic pressure. Under compression in-plane loading, $\bar{N}_0 = -3\pi^2$

and under low values of dynamic pressure the panel experiences static buckling as shown in Fig. 9. As the dynamic pressure increases the panel enters a stable state until the dynamic pressure reaches the critical value, λ_{cr}, above which the panel exhibits LCO. A three-dimensional diagram demonstrating the time evolution of LCO amplitude and their dependence on the dynamic pressure is shown in Fig. 10 for zero in-plane loading and same parameters as in the previous figures.

Under the relaxation curve shown in Fig. 11(a), the time history record of the total deflection at $x/a = 0.75$ is shown in Fig. 11(b) for in-plane compression loading, $\bar{N}_0 = -5.8\pi^2$, and dynamic pressure, $\lambda = 200$. Over the whole time domain, the panel experiences two different regimes of oscillations, namely the growing amplitude LCO, and chaotic oscillations. Fig. 12 shows the time history records of the panel deflection for two-, four-, and six-mode interactions. The purpose of this figure is to show that six-mode expansion provides satisfactory convergence. It is seen that two-mode expansion provides over estimate of the panel deflection. The difference between four and six mode expansion is very small and this supports the early claim of six-mode convergence (Dowell, 1982) for the equations of motion with constant coefficients.

Chaotic flutter is usually detected by estimating the largest value of the Lyapunov exponent. Lyapunov exponent measures the rate at which nearby trajectories converge or diverge, and are numerically calculated using the algorithm of Wolf et al. (1985). Eqs. (14) may be rewritten in terms of a set of first-order differential equations in the form

$$\dot{\boldsymbol{x}} = \boldsymbol{f}(\boldsymbol{x}; t), \tag{19}$$

where $\boldsymbol{x} = \{\boldsymbol{q}, \dot{\boldsymbol{q}}\}^{\mathrm{T}}$ is the state-space vector, where T denotes transpose and $\boldsymbol{f}$ describes the nonlinear behavior of the system. Let $\boldsymbol{x}^*(t; \boldsymbol{x}_0)$ be the reference solution of system (19), where $\boldsymbol{x}_0$ is the vector of initial conditions. In order to find the variation of trajectories in the neighborhood of the reference trajectory $\boldsymbol{x}^*(t)$, at each time step t_k we introduce the corresponding linearized equation

$$\dot{\boldsymbol{y}} = \boldsymbol{F}(\boldsymbol{x}^*(t_k))\boldsymbol{y}, \tag{20}$$

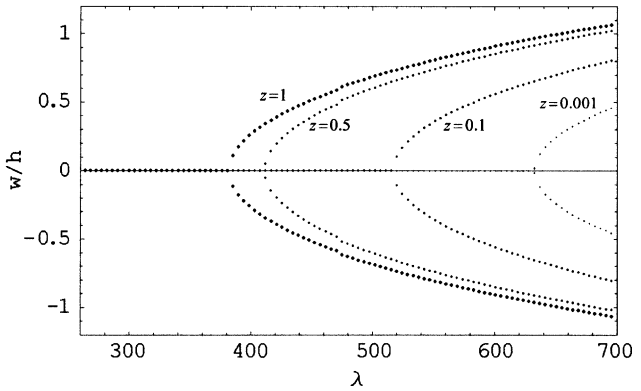

Fig. 8. Bifurcation diagram for different values of relaxation parameter for $\zeta = 0.0001$, $\hat{\zeta} = 0.1$, $\bar{p}_0 = 0$, and $\bar{N}_0 = 0$.

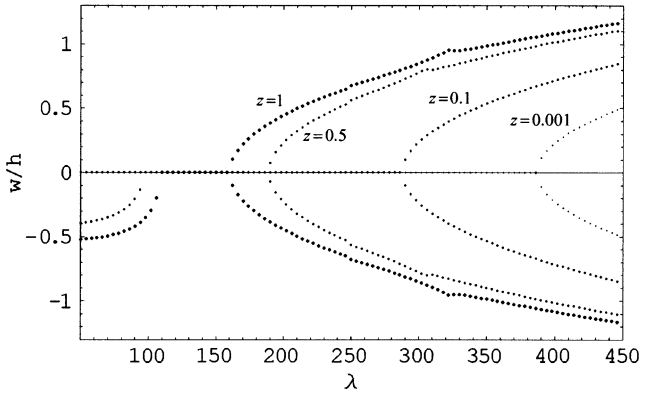

Fig. 9. Bifurcation diagram for different values of relaxation parameter for $\zeta = 0.0001$, $\hat{\zeta} = 0.1$, $\bar{p}_0 = 0$, and $\bar{N}_0 = -3\pi^2$.

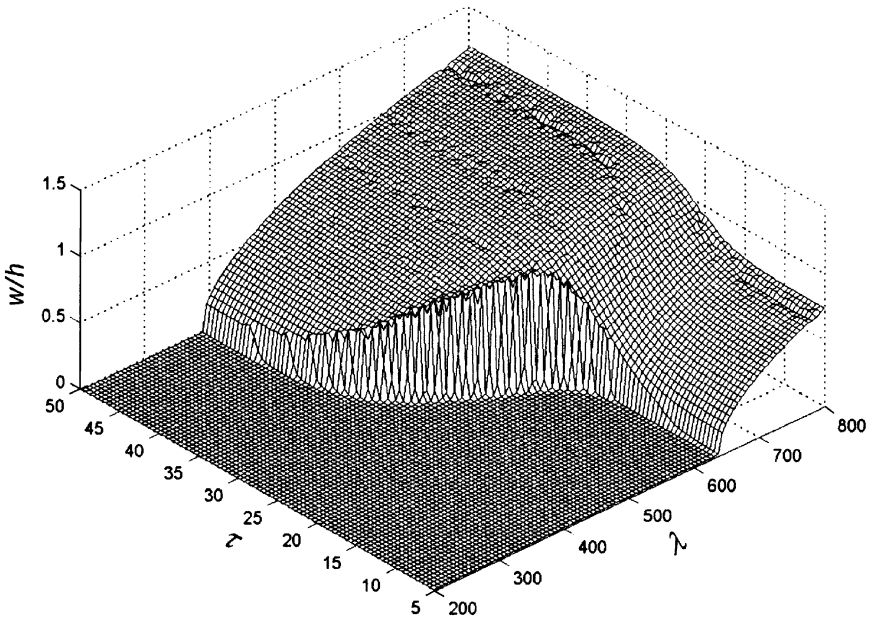

Fig. 10. Three-dimensional plots of amplitude time evolutions and their dependence on dynamic pressure for $\zeta = 0.0001$, $\hat{\zeta} = 0.1$, $\bar{p}_0 = 0.0$, and $\bar{N}_0 = 0$.

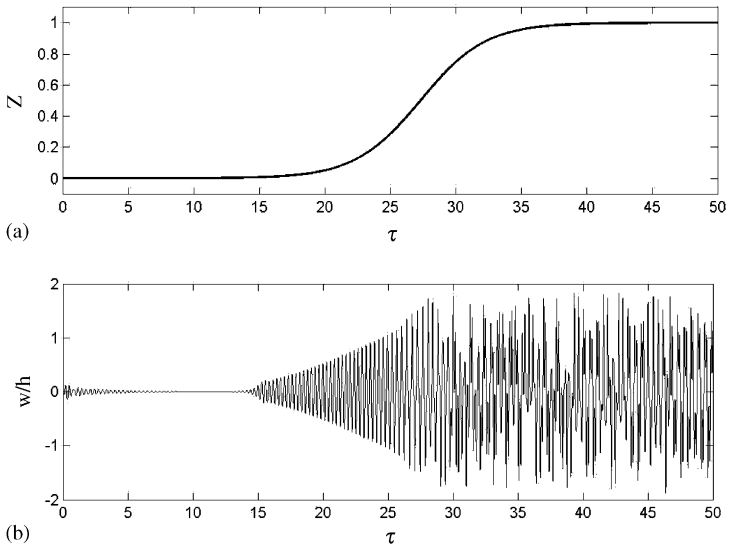

Fig. 11. (a) Relaxation of boundary conditions and (b) time history record of panel deflection at $x/a = 0.75$, for $\zeta = 0.0001$, $\bar{p}_0 = 0$, $\hat{\zeta} = 0.1$, $\bar{N}_0 = -5.8\pi^2$, and $\lambda = 200$.

where $\boldsymbol{F}(\boldsymbol{x}^*(t_k))$ is the $n \times n$ Jacobian matrix of the function $\boldsymbol{f}$ evaluated at the reference solution $\boldsymbol{x}^*(t_k)$. The jth Lyapunov exponent can be obtained as an average increment of variation vector $\boldsymbol{y}_j(t)$ during the test time Δt:

$$\lambda_j = \frac{1}{K\Delta t}\sum_{k=1}^{K} \ln \frac{\|y_j(t; t_k)\|}{\|y_j(0; t_k)\|}, \tag{21}$$

where $\|\cdot\|$ denotes vector norm and K is the number of integrations of Eqs. (19) and (20) over successive time intervals Δt. In the present study, Lyapunov exponents are estimated using a nondimensional time increment $\Delta\tau = 0.0001$. The

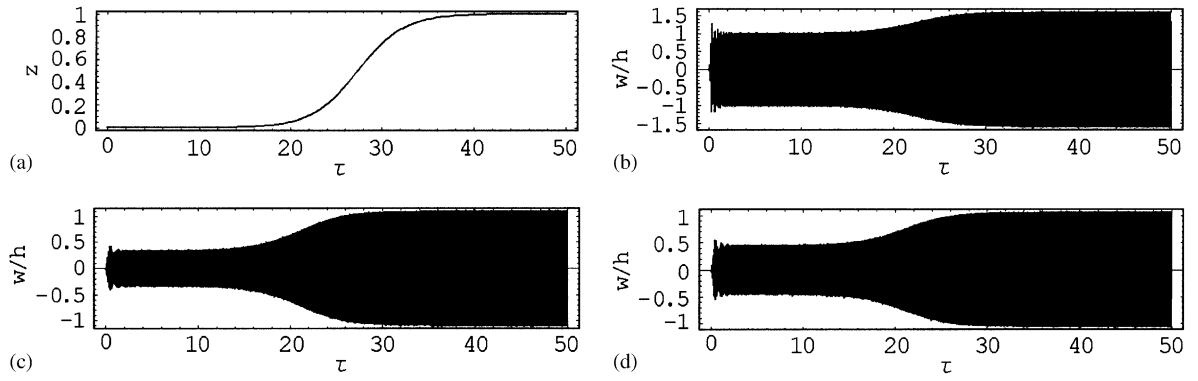

Fig. 12. (a) Relaxation of boundary conditions and time history records of the panel deflection showing convergence of the numerical results as the number of modes increases, (b) two-mode interaction, (c) four-mode interaction, and (d) six-mode interaction. $\zeta = 0.0001$, $\hat{\zeta} = 0.1$, $\bar{p}_0 = 0$, $\bar{N}_0 = -6\pi^2$, and $\lambda = 200$.

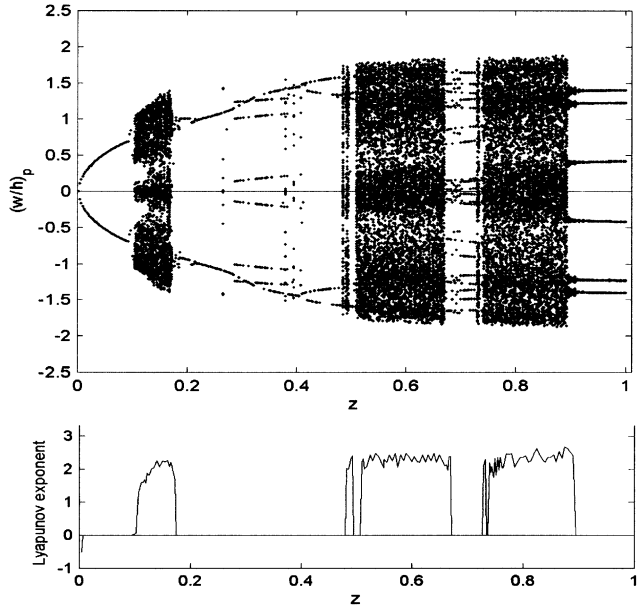

Fig. 13. Bifurcation diagram and the corresponding largest Lyapunov exponent for $\bar{p}_0 = 0$, $\bar{N}_0 = -5.8\pi^2$, $\zeta = 0.0001$, $\hat{\zeta} = 0.1$, and $\lambda = 200$.

computation starts after $\tau = 100$ and continues up to $\tau = 1000$. Fig. 13 shows some regions of relaxation parameter over which the Lyapunov exponent is positive implying the existence of chaotic flutter. Note that extreme positive values of Lyapunov exponent are found for period-n flutter regimes.

The bifurcation diagram shown in Fig. 13 is obtained by plotting the first return points of the panel amplitude for in-plane load parameter $\bar{N}_0 = -5.8\pi^2$, damping factor $\zeta = 0.0001$, static pressure $\bar{p}_0 = 0$, mass ratio parameter $\hat{\zeta} = 0.1$, and dynamic pressure $\lambda = 200$. The relaxation parameter varies between $z = 0.0025$ and $z = 1$ with an increment of $\Delta z = 0.0025$. It is seen that for relatively small values of relaxation parameter, $z < 0.105$, the panel experiences symmetric LCO with increasing amplitude as the relaxation parameter increases from the absolute clamped case, $z = 0$. The figure may be classified into the following regimes:

$0.001 \leqslant z \leqslant 0.0925$ period-one, symmetric
$0.0925 < z \leqslant 0.1025$ period-one, asymmetric
$0.1025 < z \leqslant 0.1700$ Chaos
$0.1700 < z \leqslant 0.1850$ period-two, mixture of symmetric and asymmetric

$0.1850 < z \leqslant 0.2625$ period-one, symmetric
$z = 0.2650$ period-five, symmetric
$0.2650 < z \leqslant 0.2850$ period-one, symmetric
$0.2850 < z \leqslant 0.3775$ period-one, two, and three, symmetric and asymmetric
$z = 0.3800$ period-eight, symmetric
$0.3800 < z \leqslant 0.3925$ period-one and two, symmetric
$z = 0.3950$ period-seven, symmetric
$0.3950 < z \leqslant 0.4025$ period-one, symmetric
$z = 0.4050$ period-four, symmetric
$0.4050 < z \leqslant 0.4825$ period-one, asymmetric and asymmetric
$0.4825 < z \leqslant 0.4950$ Chaos
$0.4950 < z \leqslant 0.5075$ period-doubling, asymmetric
$0.5075 < z \leqslant 0.6700$ Chaos
$0.6700 < z \leqslant 0.7275$ period-four and seven, symmetric and asymmetric
$0.7275 < z \leqslant 0.7325$ Chaos
$0.7325 < z \leqslant 0.7375$ period-six, asymmetric
$0.7375 < z \leqslant 0.8925$ Chaos
$0.8925 < z \leqslant 1$ period-three, symmetric.

For selected values of relaxation parameter, the phase plots are shown in Fig. 14. The corresponding FFT plots are shown in Fig. 15 and reveal n spikes for those period-n regimes and continuous spectrum for the chaotic motion.

Fig. 16 shows the bifurcation diagram and the corresponding Lyapunov exponent for $\lambda = 250$ and $N_0 = -6\pi^2$. The switching from symmetric to asymmetric LCO is more visible over the region $0.15 < z < 0.37$. After a window of symmetric LCO, the motion becomes chaotic ($z > 0.6325$) with the increasing of Lyapunov exponent as the relaxation

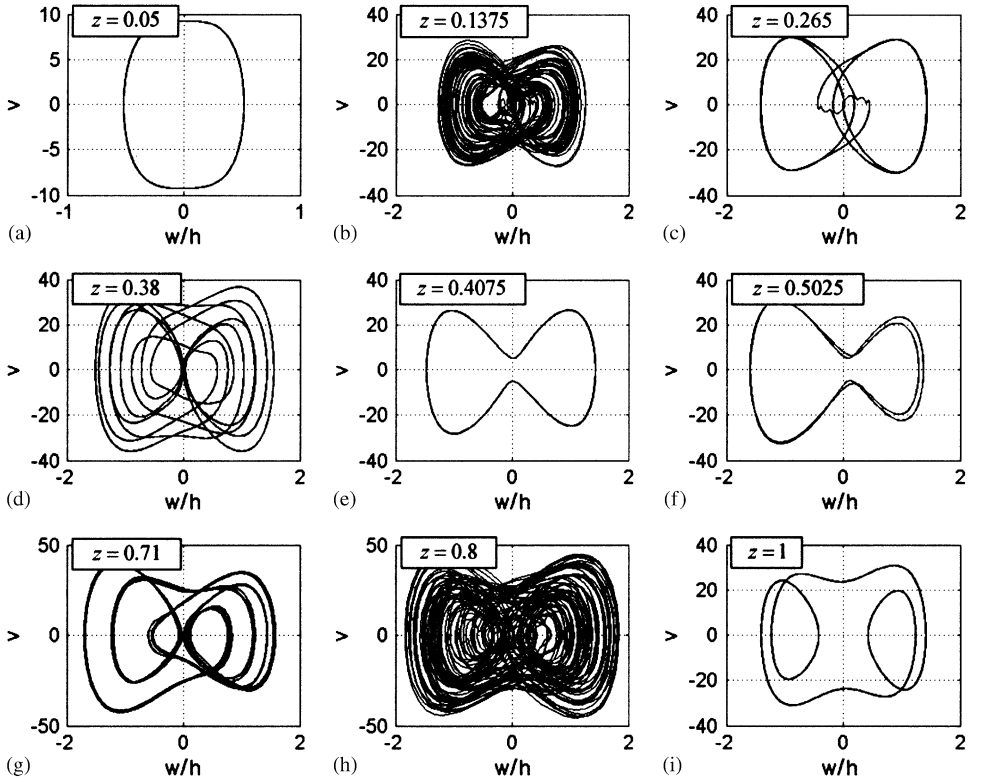

Fig. 14. Phase plots for $\zeta = 0.0001$, $\bar{p}_0 = 0$, $\hat{\zeta} = 0.1$, $\bar{N}_0 = -5.8\pi^2$, and $\lambda = 200$ corresponding to Fig. 13 for: (a) $z = 0.05$; (b) $z = 0.1375$; (c) $z = 0.265$; (d) $z = 0.38$; (e) $z = 0.4075$; (f) $z = 0.5025$; (g) $z = 0.71$; (h) $z = 0.8$; (e) $z = 1$.

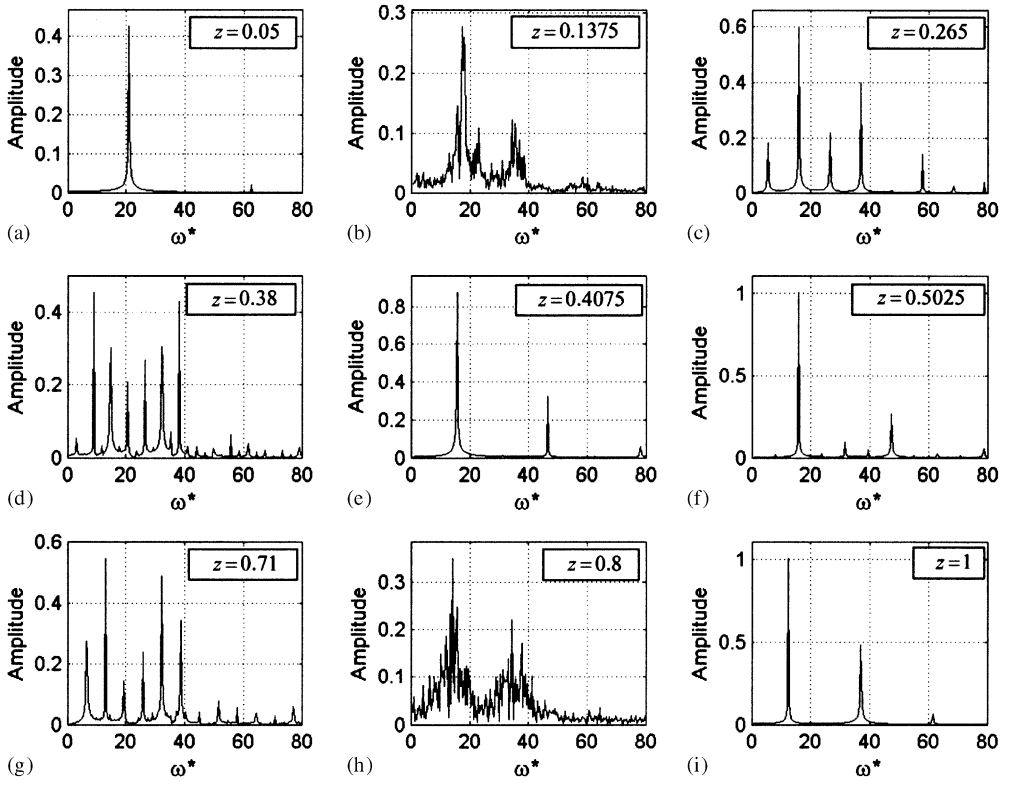

Fig. 15. FFT plots for $\zeta = 0.0001$, $\bar{p}_0 = 0$, $\hat{\zeta} = 0.1$, $\bar{N}_0 = -5.8\pi^2$, and $\lambda = 200$ corresponding to Fig. 13 for: (a) $z = 0.05$; (b) $z = 0.1375$; (c) $z = 0.265$; (d) $z = 0.38$; (e) $z = 0.4075$; (f) $z = 0.5025$; (g) $z = 0.71$; (h) $z = 0.8$; (e) $z = 1$.

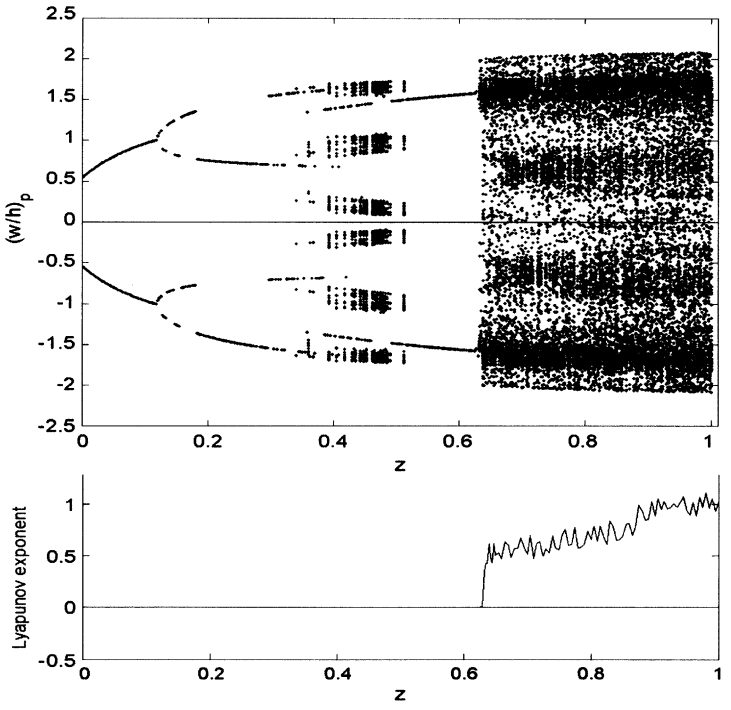

Fig. 16. Bifurcation diagram of the first return and largest Lyapunov exponent for $\zeta = 0.0001$, $\bar{p}_0 = 0$, $\hat{\zeta} = 0.1$, $\bar{N}_0 = -6\pi^2$, and $\lambda = 250$.

parameter increases. Switching between symmetric and asymmetric LCO, together with cascades of quasi-periodic motion, and chaotic flutter with windows of periodicity make the panel behavior very complex.

Figs. 13 and 16 reveal only a partial view of the route to chaotic flutter during relaxation. To have a global picture over the parametric space of dynamic pressure and relaxation parameter for given values of in-plane load and relaxation parameter, the boundaries of chaotic flutter are shown in Fig. 17 for two values of $\bar{N}_0$ and two values of ζ. The dynamic pressure varies from $\lambda = 100$ to 300 with a step size $\Delta\lambda = 5$, and relaxation parameter varies from $z = 0$ to $z = 1$ with step size $\Delta z = 0.05$ so that each map is represented by $41 \times 22 = 902$ points. Lyapunov exponent is computed for each set of parameters. A positive Lyapunov exponent indicates chaotic flutter, which is labeled by a black dot. If all exponents are negative, the panel equilibrium position is stable. If the largest Lyapunov exponent is zero the panel experiences a stable limit cycle. Both negative and zero Lyapunov exponents are labeled by a blank space. Fig. 17(a) shows chaos boundaries for $\bar{N}_0 = -6\pi^2$ and small damping ratio, $\zeta = 0.0001$. The motion is regular for $z < 0.1$. The relaxation process increases the chaos occurrence but not monotonically; instead, a complex pattern is observed. A higher in-plane load enlarges the chaos boundaries as shown in Fig. 17(c); however, the switching of windows with regular and chaotic motions is still visible. By maintaining the same in-plane load and increasing the damping ratio to $\zeta = 0.001$, the chaos boundaries are reduced considerably, especially for lower z, as shown in Figs. 17(b) and (d).

With reference to the path line A at $\bar{N}_0 = -6\pi^2$ shown in Fig. 7, we consider the panel dynamic behavior in terms of the bifurcation diagram and Lyapunov exponent, shown in Fig. 18 for relaxation parameter $z = 1$. The aerodynamic pressure, λ, is taken as the control parameter. A similar analysis is found in Epureanu et al. (2004) for a simply supported panel without structural damping. The dynamic pressure varies between $\lambda = 100$ and $\lambda = 300$ with a step increment of $\Delta\lambda = 0.25$. The bifurcation diagram begins with the buckled state of the panel up to $\lambda = 109$. The chaotic motion over the region $109.5 < \lambda < 152.5$ is followed by a region of multi-period oscillations up to $\lambda = 173$. Another window with chaotic motion is found over the range $173 < \lambda \leqslant 192$, followed by a wide window with period three motion. Increasing the aerodynamic pressure, the motion is chaotic but the chaos intensity decreases as suggested by the decreasing value of Lyapunov exponent. For $\lambda > 288$, the panel experiences LCO with increasing amplitude. Fig. 19 depicts the bifurcation diagram and corresponding Lyapunov exponent for the same path A, but with relaxation parameter $z = 0.1$. As a distinct feature, it is observed that the motion is more sensitive to the change of control parameter over the dynamic pressure range $120.5 \leqslant \lambda \leqslant 156$. With the reference to the corresponding Lyapunov exponent, the panel motion exhibits a cascade of alternating chaotic and periodic oscillations. The character of the motion is changed abruptly over a small increment of λ.

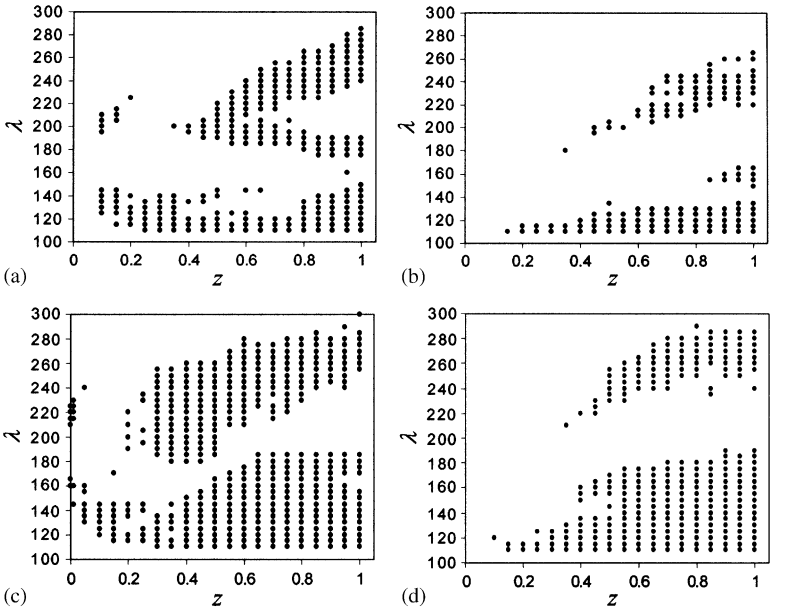

Fig. 17. Chaos boundaries for $z = 1$, $\hat{\zeta} = 0.1$, $\bar{p}_0 = 0$: (a) $\bar{N}_0 = -6\pi^2$, $\zeta = 0.0001$; (b) $\bar{N}_0 = -6\pi^2$, $\zeta = 0.001$; (c) $\bar{N}_0 = -6.8\pi^2$, $\zeta = 0.0001$; (d) $\bar{N}_0 = -6.8\pi^2$, $\zeta = 0.001$.

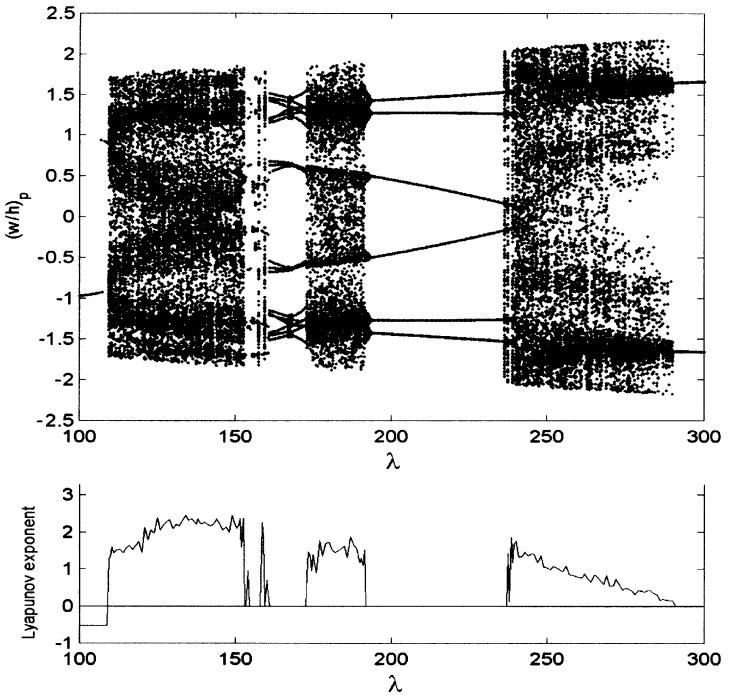

Fig. 18. Bifurcation diagram of the first return and largest Lyapunov exponent along the path line A of Fig. 7, for $\zeta = 0.0001$, $\bar{p}_0 = 0$, $\hat{\zeta} = 0.1$, $\bar{N}_0 = -6\pi^2$, and $z = 1$.

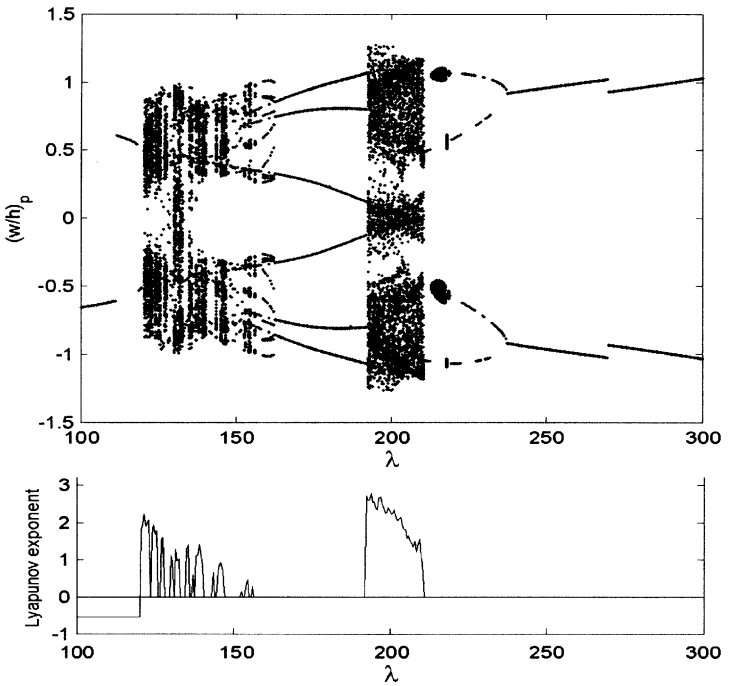

Fig. 19. Bifurcation diagram of the first return and largest Lyapunov exponent along the path line A of Fig. 7 for $\zeta = 0.0001$, $\bar{p}_0 = 0$, $\hat{\zeta} = 0.1$, $\bar{N}_0 = -6\pi^2$, and $z = 0.1$.

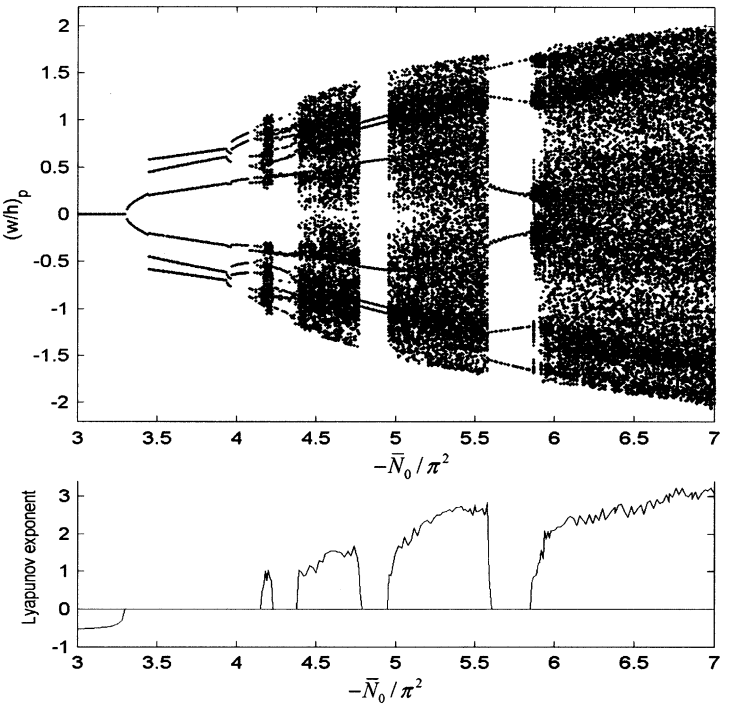

Fig. 20. Bifurcation diagram of the first return and Lyapunov exponent along the path line B of Fig. 7 for $\zeta = 0.0001$, $\bar{p}_0 = 0$, $\hat{\zeta} = 0.1$, $\lambda = 140$, and $z = 1$.

With reference to the path line B at $\lambda = 140$ of Fig. 7, we consider the dynamic behavior of the panel by varying the in-plane load N_0. The bifurcation diagram illustrated in Fig. 20 is determined for relaxation parameter, $z = 1$. It is seen that the panel is stable for small in-plane load up to $\bar{N}_0 = 3.3$, above which it experiences LCO over the range $3.3 < \bar{N}_0 < 3.45$. At $\bar{N}_0 = 3.45$ the panel experiences secondary bifurcation with symmetric period-3 oscillations. Increasing the in-plane load, the motion switches between asymmetric and symmetric multi-harmonic oscillations. Further increase of the in-plane loading results in a chaotic motion with three windows of periodicity: $4.22 < \bar{N}_0 < 4.39$, $4.77 < \bar{N}_0 < 4.96$, and $5.5 < \bar{N}_0 < 5.87$.

For the same set of parameters, the response may be different depending on initial conditions. This is true not only for the chaotic motion but also for the periodic oscillations. Fig. 21 shows phase portraits for four different sets of parameters. Each phase portrait is drawn for two different initial conditions (1) $q_1(\tau = 0) = 0.1$, $q_i(\tau = 0) = 0$, $i = 2, \ldots, 6$, $\dot{q}_i = 0$, $i = 1, \ldots, 6$, and (2) $q_1(\tau = 0) = 1$, $q_i(\tau = 0) = 0$, $i = 2, \ldots, 6$, $\dot{q}_i = 0$, $i = 1, \ldots, 6$, respectively. One can observe from Figs. 21(a) and (b) that multi-periodic oscillations corresponding to initial condition set (1) and becomes a period-3 oscillation in the case of initial condition set (2). In both cases, the response is symmetric. For other sets of parameters two asymmetric solutions coexist as shown in Figs. 21(c) and (d). The panel response follows one of these solutions, depending on the initial condition. The coexistence of symmetric and asymmetric LCO is better observed in the bifurcation diagram shown in Fig. 22 for $\bar{N}_0 = -6\pi^2$, and $z = 0.1$. The response is asymmetric over the range $233 < \lambda \leqslant 237.5$ depending on the initial conditions; after that, the response becomes symmetric, independent of the initial conditions.

4.2. Time–frequency analysis

The ultimate decision on whether the motion is chaotic or not is given by the existence of a positive Lyapunov exponent. However, the Lyapunov exponent is characterized by a slow convergence and requires long time simulations and large computation resources. Time limitations may be critical, especially when experimental data is available for a limited time history record. Therefore, at least for preliminary investigations, the information from the bifurcation diagram, phase plot and power spectrum is generally sufficient. The relaxation of the boundary conditions results in time variation of the panel natural frequencies, and thus, the flutter becomes nonstationary. The Fourier transform

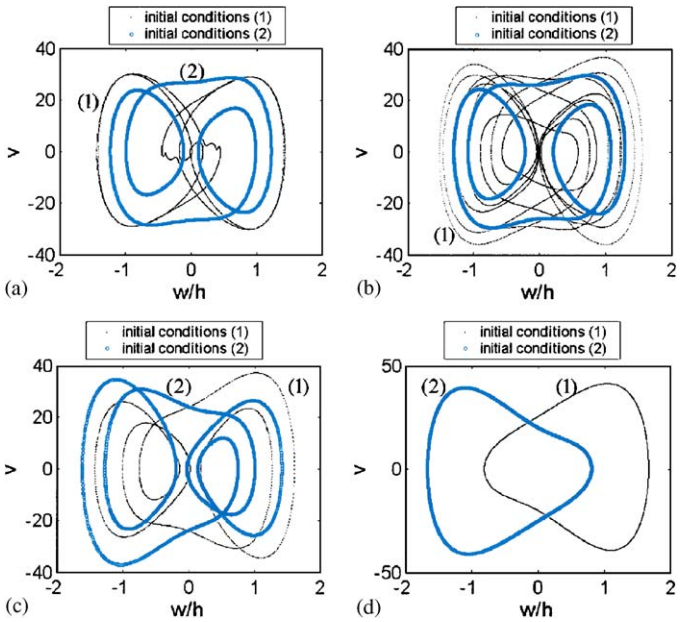

Fig. 21. Phase diagrams for $\zeta = 0.0001$, $\bar{p}_0 = 0$, $\hat{\zeta} = 0.1$, for two sets of initial conditions: (1) $q_1(\tau = 0) = 0.1$, $q_i(\tau = 0) = 0$, $i = 2, \ldots, 6$, $\dot{q}_i = 0$, $i = 1, \ldots, 6$; (2) $q_1(\tau = 0) = 1$, $q_i(\tau = 0) = 0$, $i = 2, \ldots, 6$, $\dot{q}_i = 0$, $i = 1, \ldots, 6$. (a) $\lambda = 200$, $\bar{N}_0 = -5.8\pi^2$, $z = 0.265$; (b) $\lambda = 200$, $\bar{N}_0 = -5.8\pi^2$, $z = 0.38$; (c) $\lambda = 179$, $\bar{N}_0 = -6\pi^2$, $z = 0.5$; (d) $\lambda = 270$, $\bar{N}_0 = -6\pi^2$, $z = 0.5$.

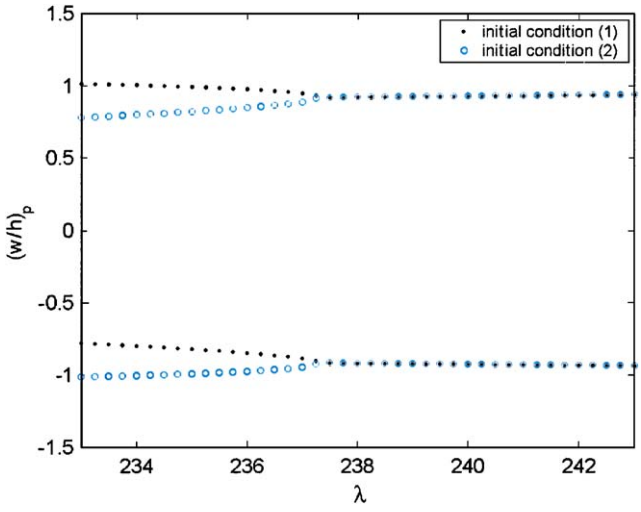

Fig. 22. Section of bifurcation diagram of the first return for $\zeta = 0.0001$, $\bar{p}_0 = 0$, $\hat{\zeta} = 0.1$, $\bar{N}_0 = -6\pi^2$, and $z = 0.1$ for initial conditions: (1) $q_1(\tau = 0) = 0.1$, $q_i(\tau = 0) = 0$, $i = 2, \ldots, 6$, $\dot{q}_i = 0$, $i = 1, \ldots, 6$, and (2) $q_1(\tau = 0) = 1$, $q_i(\tau = 0) = 0$, $i = 2, \ldots, 6$, $\dot{q}_i = 0$, $i = 1, \ldots, 6$.

does not reveal the time dependency of the frequency of panel oscillations. The present work will adopt two techniques usually used for nonstationary signal analysis. These are the windowed Fourier transform, known as the spectrogram, originally developed by Gabor (1946) and the Morlet wavelet transform. Note that both transforms have time–frequency resolution limitations for the determination of the instantaneous frequencies. The windowed Fourier transform relies on the selected length of the window. Any special features occurring during short time-scales smaller than the length of the window, or with smaller frequencies than those contained in the window, are lost and cannot be captured by the windowed Fourier transform. On the other hand, the wavelet transform has the advantage in that it

follows the rapid variations of the instantaneous frequencies since it adjusts the length of the window according to the frequency content of the signal.

For the case of the short time Fourier transform, real and symmetric window $g(t) = g(-t)$ is translated by τ and modulated by the frequency ϖ,

$$g_{\tau,\varpi}(t) = \mathrm{e}^{\mathrm{i}\varpi t} g(t-\tau), \quad \|g\| = 1 \quad \text{and} \quad \|g_{\tau,\varpi}\| = 1. \tag{22}$$

The windowed Fourier transform, known also as the short–time Fourier transform, of the panel deflection $q_i(t)$ is

$$S\bar{w}(\tau,\varpi) = \int_{-\infty}^{\infty} \bar{w}(t) g(t-\tau) \mathrm{e}^{-\mathrm{i}\varpi t}\, \mathrm{d}t. \tag{23}$$

In the present work, the Kaiser window function is used. It has the following form:

$$g(t) = \begin{cases} \dfrac{I_0\left(\beta\sqrt{1-(t/T)^2}\right)}{I_0(\beta)} & |t| < T, \\ 0 & \text{otherwise}, \end{cases} \tag{24}$$

where I_0 is the modified Bessel function of order zero and of first kind, β is a parameter that governs the shape of the window, and T is the signal total time. The spectrogram measures the energy density of the flutter deflection $\bar{w}$ in the time–frequency neighborhood of (τ, ϖ) given by

$$P_S\bar{w}(\tau,\varpi) = |S\bar{w}(\tau,\varpi)|^2 = \left| \int_{-\infty}^{\infty} \bar{w}(t) g(t-\tau) \mathrm{e}^{-\mathrm{i}\varpi t}\, \mathrm{d}t \right|^2. \tag{25}$$

Figs. 23(a) and (b) show two cases of the FFT plots and spectrograms of the panel total deflection time history records for (a) $\lambda = 700$, and $\zeta = 0.0001$, and (b) $\lambda = 700$, and $\zeta = 0.02$, respectively. For low damping, Fig. 23(a) shows that the panel frequency decreases with time as the panel boundary conditions approach the case of simple supports. On the other hand, as the damping increases, the panel frequency increases with time. There are two factors competing with each other, namely, the structural geometric nonlinearity and the relaxation in the boundary conditions. By increasing

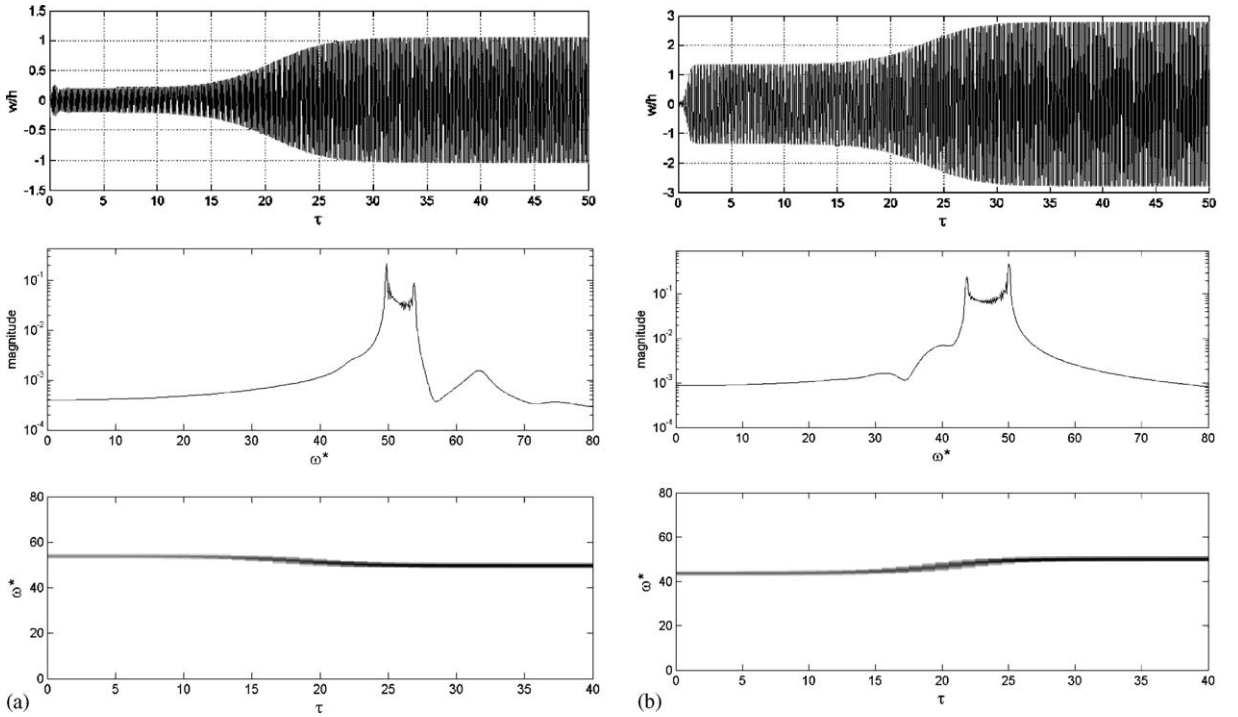

Fig. 23. FFT plots and spectrograms for $\bar{p}_0 = 0$, $\bar{N}_0 = 0$, $\hat{\zeta} = 0.1$. (a) $\lambda = 700$, $\zeta = 0.0001$, (b) $\lambda = 700$, $\zeta = 0.02$.

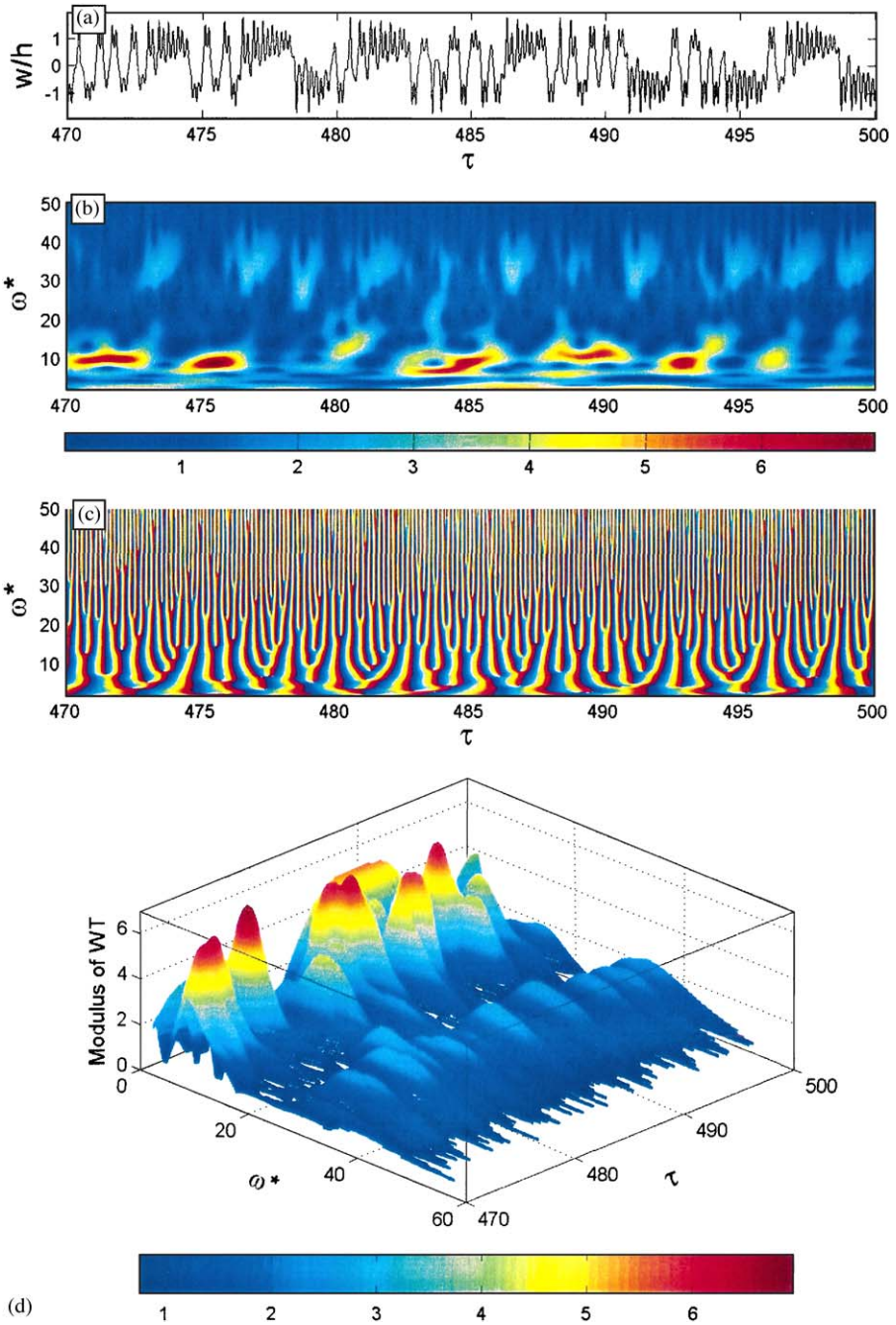

Fig. 24. (a) Time history, (b) modulus of WT, (c) phase of WT, (d) three-dimensional plot of modulus of WT for $\zeta = 0.0001$, $\bar{p}_0 = 0$, $\hat{\zeta} = 0.1$, $\lambda = 132$, $\bar{N}_0 = -6\pi^2$, and $z = 1$.

the damping factor, the structural geometric nonlinearity overcomes the influence of relaxation, and the frequency increases as shown in Fig. 23(b).

Alternatively, we will use the continuous wavelet transform technique to present the time history records as a two-dimensional function of time and frequency to reveal the wavelet modulus and phase. A wavelet is a function $\psi(t) \in \mathbf{L}^2(\mathbb{R})$ with zero average. A family of time–frequency atoms is obtained by scaling ψ by s and translating it by τ

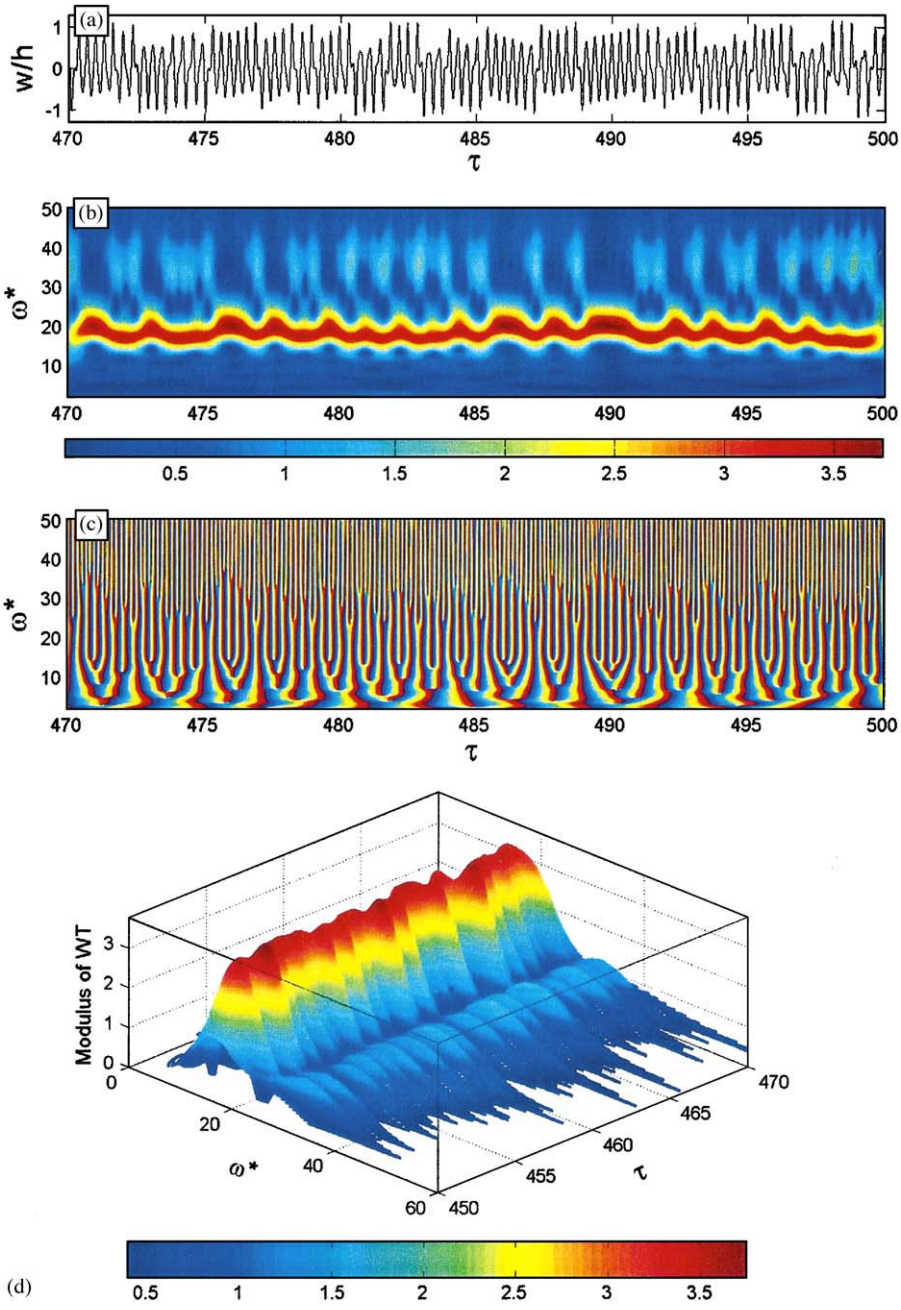

Fig. 25. (a) Time history, (b) modulus of WT, (c) phase of WT, (d) three-dimensional plot of modulus of WT for $\zeta = 0.0001$, $\bar{p}_0 = 0$, $\hat{\zeta} = 0.1$, $\lambda = 203.5$, $\bar{N}_0 = -6\pi^2$, and $z = 0.1$.

(Mallat, 1999)

$$\psi_{\tau,s}(t) = \frac{1}{\sqrt{s}}\psi\left(\frac{t-\tau}{s}\right), \quad \|\psi_{u,s}\| = 1. \tag{26}$$

The wavelet transform (WT) of the signal $\bar{w} \in \mathbf{L}^2(\mathbb{R})$ at time τ and scale s is

$$W\bar{w}(\tau, s) = \langle \bar{w}, \psi_{u,s} \rangle = \int_{-\infty}^{\infty} \bar{w}(t)\frac{1}{\sqrt{s}}\psi^*\left(\frac{t-\tau}{s}\right) \mathrm{d}t. \tag{27}$$

The mother wavelet for the Morlet is given by the following function:

$$\psi(t) = \pi^{-1/4} e^{i\omega_0|t|} e^{-|t|^2/2}. \tag{28}$$

The modulus of the wavelet transform is defined as

$$|W_\psi^{\bar{w}}(\tau, s)| = \sqrt{(\mathrm{Re}[W_\psi^{\bar{w}}(\tau, s)])^2 + (\mathrm{Im}[W_\psi^{\bar{w}}(\tau, s)])^2}, \tag{29}$$

and the phase is

$$\phi(\tau, s) = \tan^{-1}\left(\frac{\mathrm{Im}[W_\psi^{\bar{w}}(\tau, s)]}{\mathrm{Re}[W_\psi^{\bar{w}}(\tau, s)]}\right). \tag{30}$$

The square of the modulus $|W_\psi^{\bar{w}}(\tau, s)|^2$ represents the energy density distribution of the signal over the time-scale plane, (τ, s). On the other hand, the phase measures the relative position of the signal and its analyzing wavelet. The graphical representation of the WT modulus in time-scale plane is called *scalogram*. Fig. 24 shows the time history, scalogram, and wavelet phase for fixed parameters $\lambda = 132$, $\bar{N}_0 = -6\pi^2$, and $z = 1$. The scalogram shown in Fig. 24(b) illustrates a large spectrum of frequencies randomly distributed in time. According to Newland (1999a, b), the absolute phase is not a useful indicator because it depends on wavelet location. However, the rate of change of phase with time in the same frequency band is an interesting parameter because it is constant when the signal is harmonic of fixed frequency and phase. Fig. 24(c) shows the projection of phase on the frequency–time plane and one can see the evolution of phase with time does not maintain a constant value. A better visualization of time-frequency evolution of the wavelet modulus is illustrated in the three-dimensional plot (Fig. 24(d)). Similarly, Fig. 25 shows the time history, wavelet modulus and wavelet phase for fixed parameters $\lambda = 203.5$, $\bar{N}_0 = -6\pi^2$, and $z = 0.1$. The wavelet scalogram shows a band of frequencies varying about a dominant component of $\omega^* = 20$ dimensionless frequency. In addition, intermittent higher frequency components randomly distributed in time are observed. Although the time history shows a certain degree of repeatability, the motion is still chaotic. Compared to the Lyapunov exponent, the wavelet transform is suitable for a short time domain analysis. However, the wavelet analysis cannot provide a quantitative tool to measure chaos.

5. Conclusions

The nonlinear flutter of a two-dimensional panel exposed to supersonic gas flow involving six-mode interaction is studied in the presence of nonideal boundary conditions. The deterministic study includes stability analysis in terms of dynamic pressure, relaxation parameter, damping ratio, and in-plane loading. For in-plane loading below the critical buckling value, the panel experiences LCO above a critical aerodynamic pressure governed by the relaxation parameter. For compressive in-plane loads, the panel experiences periodic, quasi-periodic and chaotic oscillations, depending on the values of dynamic pressure, relaxation parameter and damping ratios. Bifurcation diagrams of the first return and the associated largest Lyapunov exponent are estimated by taking the dynamic pressure or the relaxation parameter or the in-plane loading as control parameters. The chaos regions represented by the largest positive Lyapunov exponent were found to be reduced for a small relaxation parameter. The initial conditions were found to affect the behavior of the panel flutter in the periodicity and symmetry of oscillations. The time–frequency analysis of the panel flutter was estimated using the techniques of the spectrogram and the Morlet wavelet transform. The importance of these transforms is to reveal the degree of nonstationarity of panel flutter in terms of frequency time variations and nonlinear behavior.

Acknowledgments

This research is supported by grants from the Institute for Manufacturing Research and the Air Force Office of Scientific Research under Grant F49620-03-1-0229. Dr Dean Mook is the AFOSR Program Director. The authors would like to thank the reviewers for their valuable comments.

Appendix

This appendix gives the matrices of Eq. (14) and samples of their elements, namely:

$$M(\tau)=\begin{bmatrix} 1 & 0 & m_{13} & 0 & m_{15} & 0 \\ 0 & 1 & 0 & m_{24} & 0 & m_{26} \\ m_{31} & 0 & 1 & 0 & m_{35} & 0 \\ 0 & m_{42} & 0 & 1 & 0 & m_{46} \\ m_{51} & 0 & m_{53} & 0 & 1 & 0 \\ 0 & m_{52} & 0 & m_{64} & 0 & 1 \end{bmatrix}, \quad m_{13}(\tau)=-\frac{9}{4[3+\pi^2(1+6z(\tau))]},$$

$$C=\begin{bmatrix} \zeta b_{11}+\hat{\zeta}\sqrt{\lambda} & 0 & \zeta b_{12}+\hat{\zeta}b_{13}\sqrt{\lambda} & 0 & \zeta b_{14}+\hat{\zeta}b_{15}\sqrt{\lambda} & 0 \\ 0 & \zeta b_{21}+\hat{\zeta}\sqrt{\lambda} & 0 & \zeta b_{22}+\hat{\zeta}b_{23}\sqrt{\lambda} & 0 & \zeta b_{24}+\hat{\zeta}b_{25}\sqrt{\lambda} \\ \zeta b_{31}+\hat{\zeta}b_{32}\sqrt{\lambda} & 0 & \zeta b_{33}+\hat{\zeta}\sqrt{\lambda} & 0 & \zeta b_{34}+\hat{\zeta}b_{35}\sqrt{\lambda} & 0 \\ 0 & \zeta b_{41}+\hat{\zeta}b_{42}\sqrt{\lambda} & 0 & \zeta b_{43}+\hat{\zeta}\sqrt{\lambda} & 0 & \zeta b_{44}+\hat{\zeta}b_{45}\sqrt{\lambda} \\ \zeta b_{51}+\hat{\zeta}b_{52}\sqrt{\lambda} & 0 & \zeta b_{53}+\hat{\zeta}b_{54}\sqrt{\lambda} & 0 & \zeta b_{55}+\hat{\zeta}\sqrt{\lambda} & 0 \\ 0 & \zeta b_{61}+\hat{\zeta}b_{62}\sqrt{\lambda} & 0 & \zeta b_{63}+\hat{\zeta}b_{64}\sqrt{\lambda} & 0 & \zeta b_{65}+\hat{\zeta}\sqrt{\lambda} \end{bmatrix},$$

$$b_{11}(\tau)=\frac{\pi^4[51+\pi^2(1+6z(\tau))]}{3+\pi^2(1+6z(\tau))},$$

$$K=\begin{bmatrix} c_{11}\bar{N}_0+c_{12} & c_{13}\lambda+c_{14} & c_{15}\bar{N}_0+c_{16} & c_{17}\lambda+c_{18} & c_{19}\bar{N}_0+c_{110} & c_{111}\lambda+c_{112} \\ c_{21}\lambda+c_{22} & c_{23}\bar{N}_0+c_{24} & c_{25}\lambda+c_{26} & c_{27}\bar{N}_0+c_{28} & c_{29}\lambda+c_{210} & c_{211}\bar{N}_0+c_{212} \\ c_{31}\bar{N}_0+c_{32} & c_{33}\lambda+c_{34} & c_{35}\bar{N}_0+c_{36} & c_{37}\lambda+c_{38} & c_{39}\bar{N}_0+c_{310} & c_{311}\lambda+c_{312} \\ c_{41}\lambda+c_{42} & c_{43}\bar{N}_0+c_{44} & c_{45}\lambda+c_{46} & c_{47}\bar{N}_0+c_{48} & c_{49}\lambda+c_{410} & c_{411}\bar{N}_0+c_{412} \\ c_{51}\bar{N}_0+c_{52} & c_{53}\lambda+c_{54} & c_{55}\bar{N}_0+c_{56} & c_{57}\lambda+c_{58} & c_{59}\bar{N}_0+c_{510} & c_{511}\lambda+c_{512} \\ c_{61}\lambda+c_{62} & c_{63}\bar{N}_0+c_{64} & c_{65}\lambda+c_{66} & c_{67}\bar{N}_0+c_{68} & c_{69}\lambda+c_{610} & c_{611}\bar{N}_0+c_{612} \end{bmatrix},$$

$$c_{13}=-\frac{16(26+9\pi^2 z)}{9(3+\pi^2(1+6z))},$$

$$D=\begin{bmatrix} d_{11} & 0 & d_{13} & 0 & d_{15} & 0 \\ 0 & d_{22} & 0 & d_{24} & 0 & d_{26} \\ d_{31} & 0 & d_{33} & 0 & d_{35} & 0 \\ 0 & d_{42} & 0 & d_{44} & 0 & d_{46} \\ d_{51} & 0 & d_{53} & 0 & d_{55} & 0 \\ 0 & d_{62} & 0 & d_{64} & 0 & d_{66} \end{bmatrix},$$

$$d_{11}(\tau)=\frac{1}{60}[-15+10\pi^2(1+3z(\tau))+\pi^4(1+10z(\tau)+30z^2(\tau))]B_1,$$

$$\{eq_iq_j^2\} = \begin{Bmatrix} e_{11}q_1q_2^2 + e_{12}q_1q_3^2 + e_{13}q_1q_4^2 + e_{14}q_1q_5^2 + e_{15}q_1q_6^2 + e_{16}q_3q_1^2 + e_{17}q_3q_2^2 + e_{18}q_3q_4^2 \\ e_{21}q_2q_1^2 + e_{22}q_2q_3^2 + e_{23}q_2q_4^2 + e_{24}q_2q_5^2 + e_{25}q_2q_6^2 + e_{26}q_4q_1^2 + e_{27}q_4q_2^2 + e_{28}q_4q_3^2 \\ e_{31}q_1q_2^2 + e_{32}q_1q_3^2 + e_{33}q_1q_4^2 + e_{34}q_1q_5^2 + e_{35}q_1q_6^2 + e_{36}q_3q_1^2 + e_{37}q_3q_2^2 + e_{38}q_3q_4^2 \\ e_{41}q_2q_1^2 + e_{42}q_2q_3^2 + e_{43}q_2q_4^2 + e_{44}q_2q_5^2 + e_{45}q_2q_6^2 + e_{46}q_4q_1^2 + e_{47}q_4q_2^2 + e_{48}q_4q_3^2 \\ e_{51}q_1q_2^2 + e_{52}q_1q_3^2 + e_{53}q_1q_4^2 + e_{54}q_1q_5^2 + e_{55}q_1q_6^2 + e_{56}q_3q_1^2 + e_{57}q_3q_2^2 + e_{58}q_3q_4^2 \\ e_{61}q_2q_1^2 + e_{62}q_2q_3^2 + e_{63}q_2q_4^2 + e_{64}q_2q_5^2 + e_{65}q_2q_6^2 + e_{66}q_4q_1^2 + e_{67}q_4q_2^2 + e_{68}q_4q_3^2 \end{Bmatrix}$$
$$\begin{Bmatrix} +e_{19}q_3q_5^2 + e_{110}q_3q_6^2 + e_{111}q_5q_1^2 + e_{112}q_5q_2^2 + e_{113}q_5q_3^2 + e_{114}q_5q_4^2 + e_{115}q_5q_6^2 \\ +e_{29}q_4q_5^2 + e_{210}q_4q_6^2 + e_{211}q_6q_1^2 + e_{212}q_6q_2^2 + e_{213}q_6q_3^2 + e_{214}q_5q_4^2 + e_{215}q_6q_5^2 \\ +e_{39}q_3q_5^2 + e_{310}q_3q_6^2 + e_{311}q_5q_1^2 + e_{312}q_5q_2^2 + e_{313}q_5q_3^2 + e_{314}q_5q_4^2 + e_{315}q_5q_6^2 \\ +e_{49}q_4q_5^2 + e_{410}q_4q_6^2 + e_{411}q_6q_1^2 + e_{412}q_6q_2^2 + e_{413}q_6q_3^2 + e_{414}q_6q_4^2 + e_{415}q_6q_5^2 \\ +e_{59}q_3q_5^2 + e_{510}q_3q_6^2 + e_{511}q_5q_1^2 + e_{512}q_5q_2^2 + e_{513}q_5q_3^2 + e_{514}q_5q_4^2 + e_{515}q_5q_6^2 \\ +e_{69}q_4q_5^2 + e_{610}q_4q_6^2 + e_{611}q_6q_1^2 + e_{612}q_6q_2^2 + e_{613}q_6q_3^2 + e_{614}q_6q_4^2 + e_{615}q_6q_5^2 \end{Bmatrix},$$

$$e_{11}(\tau) = \frac{1}{240}[-15 + 40\pi^2(1 + 3z(\tau)) + 16\pi^4(1 + 10z(\tau) + 30z^2(\tau))]B_1,$$

$$\{fq_iq_jq_k\} = \begin{Bmatrix} f_{11}q_1q_2q_4 + f_{12}q_1q_2q_6 + f_{13}q_1q_3q_5 + f_{14}q_1q_4q_6 + f_{15}q_2q_3q_4 \\ f_{21}q_1q_2q_3 + f_{22}q_1q_3q_4 + f_{23}q_1q_2q_5 + f_{24}q_2q_3q_5 + f_{25}q_1q_4q_5 \\ f_{31}q_1q_2q_4 + f_{32}q_1q_2q_6 + f_{33}q_1q_3q_5 + f_{34}q_1q_4q_6 + f_{35}q_2q_3q_4 \\ f_{41}q_1q_2q_3 + f_{42}q_1q_3q_4 + f_{43}q_1q_2q_5 + f_{44}q_2q_3q_5 + f_{45}q_1q_4q_5 \\ f_{51}q_1q_2q_4 + f_{52}q_1q_2q_6 + f_{53}q_1q_3q_5 + f_{54}q_1q_4q_6 + f_{55}q_2q_3q_4 \\ f_{61}q_1q_2q_3 + f_{62}q_1q_3q_4 + f_{63}q_1q_2q_5 + f_{64}q_2q_3q_5 + f_{65}q_1q_4q_5 \end{Bmatrix}$$
$$\begin{Bmatrix} +f_{16}q_2q_3q_6 + f_{17}q_2q_4q_5 + f_{18}q_2q_5q_6 + f_{19}q_3q_4q_6 + f_{110}q_4q_5q_6 \\ +f_{26}q_2q_4q_6 + f_{27}q_3q_4q_5 + f_{28}q_1q_3q_6 + f_{29}q_3q_5q_6 + f_{210}q_1q_5q_6 \\ +f_{36}q_2q_3q_6 + f_{37}q_2q_4q_5 + f_{38}q_2q_5q_6 + f_{39}q_3q_4q_6 + f_{310}q_4q_5q_6 \\ +f_{46}q_2q_4q_6 + f_{47}q_3q_4q_5 + f_{48}q_1q_3q_6 + f_{49}q_3q_5q_6 + f_{410}q_1q_5q_6 \\ +f_{56}q_2q_3q_6 + f_{57}q_2q_4q_5 + f_{58}q_2q_5q_6 + f_{59}q_3q_4q_6 + f_{510}q_4q_5q_6 \\ +f_{66}q_2q_4q_6 + f_{67}q_3q_4q_5 + f_{68}q_1q_3q_6 + f_{69}q_3q_5q_6 + f_{610}q_1q_5q_6 \end{Bmatrix},$$

$$f_{11}(\tau) = -\frac{16}{27}(22 + 15\pi^2 z(\tau))B_1, \quad \{P(\tau)\} = \begin{Bmatrix} 2\bar{p}_0/\pi a_{11} \\ 0 \\ 3\bar{p}_0/2\pi a_{33} \\ 0 \\ 5\bar{p}_0/3\pi a_{55} \\ 0 \end{Bmatrix}, \quad a_{11}(\tau) = -\frac{1}{12}\left(1 + \frac{3}{\pi^2} + 6z(\tau)\right).$$

The complete set of coefficients $m_{ij}, b_{ij}, c_{ij}, d_{ij}, e_{ij}, f_{ij}$, and, a_{ii} is given in Beloiu (2005).

References

Ashley, H., Zartarian, G., 1956. Piston theory—a new aerodynamic tool for aeroelastician. Journal of the Aeronautical Sciences 23, 1109–1118.

Beloiu, D.M., 2005. Non-smooth dynamics of disc brake systems and aeroelastic panels. Ph.D. Dissertation, Wayne State University, Department of Mechanical Engineering, Detroit, Michigan.

Bickford, J.H., 1990. An Introduction to the Design and Behavior of Bolted Joints, second ed. Marcel Dekker, Inc., New York.

Bismarck-Nasr, M.N., Bones, C.A., 2000. Damping effect in nonlinear panel flutter. AIAA Journal 38, 711–713.

Bolotin, V.V., Grishko, A.A., Kounadis, A.N., Gantes, C.J., 1998. Non-linear panel flutter in remote postcritical domains. International Journal of Non-Linear Mechanics 33, 753–764.

Bolotin, V.V., Grishko, A.A., Panov, M.Yu., 2002. Effect of damping on the post-critical behavior of autonomous non-conservative system. International Journal of Non-Linear Mechanics 37, 1163–1179.

Brenner, M.J., 1997. Wavelet Analysis of F/A-18 Aeroelastic and Aeroservoelastic Flight Test Data, NASA TM 4793.

Brenner, M.J., 2002a. Aeroservoelastic uncertainty model identification from flight data. Journal of Guidance, Control, and Dynamics 25, 748–754.

Brenner, M.J., 2002b. Non-stationary dynamics data analysis with wavelet-SVD filtering. Mechanical Systems and Signal Processing 17, 765–786.

Dowell, E.H., 1966. Nonlinear oscillations of a fluttering plate. AIAA Journal 4 (7), 1267–1275.

Dowell, E.H., 1982. Flutter of buckled plate as an example of chaotic motion of a deterministic autonomous system. Journal of Sound and Vibration 85, 333–344.

Dowell, E.H., 1984. Observation and evolution of chaos for an autonomous system. Journal of Applied Mechanics 51, 664–673.

Epureanu, B.I., Liaosha, S.T., Païdoussis, M.P., 2004. Coherent structures and their influence on the dynamics of aeroelastic panels. International Journal of Non-Linear Mechanics 39, 977–991.

Gabor, D., 1946. Theory of communication. Journal of IEE 93, 429–457.

Ibrahim, R.A., 1987. Structural dynamics with parameter uncertainties. Applied Mechanics Reviews 40, 309–328.

Ibrahim, R.A., Pettit, C.L., 2004. Uncertainties and dynamic problems of bolted joints and other fasteners. Journal of Sound and Vibration 279, 857–936.

Ibrahim, R.A., Orono, P.O., Madaboosi, S.R., 1990. Stochastic flutter of a panel subjected to random in-plane forces, part i: two mode interaction. AIAA Journal 28, 694–702.

Ibrahim, R.A., Beloiu, D.M., Pettit, C.L., 2004. Influence of joint relaxation on deterministic and stochastic panel flutter. AIAA Journal 43 (7), 1444–1454.

Johnson, J.D., Lu, J., Dhawan, A.P., Lind, R., 2002. Real-time identification of flutter boundaries using the discrete wavelet transform. Journal of Guidance, Control, and Dynamics 25, 334–339.

Kuo, C.C., Morino, L., Dugundji, J., 1972. Perturbation and harmonic balance methods for nonlinear panel flutter. AIAA Journal 10, 1479–1484.

Kuttenkeuler, J., Ringertz, U., 1998. Aeroelastic tailoring considering uncertainties in material properties. Structural Optimization 15, 157–162.

Liaw, D.G., Yang, T.Y., 1991a. Reliability of initially compressed uncertain laminated plates in supersonic flow. AIAA Journal 29, 952–960.

Liaw, D.G., Yang, T.Y., 1991b. Reliability of uncertain laminated shells due to buckling and supersonic flutter. AIAA Journal 29, 1698–1708.

Lind, R., Brenner, M., 2000. Flutterometer: an on-line tool to predict robust flutter margins. Journal of Aircraft 37, 1105–1112.

Lindsley, N.J., Beran, P.S., Pettit, C.L., 2002a. Effects of uncertainty on nonlinear plate response in supersonic flow. Ninth AIAA Symposium on Multidisciplinary Analysis and Optimization, Atlanta, GA, Paper 2002-5600.

Lindsley, N.J., Beran, P.S., Pettit, C.L., 2002b. Effects of uncertainty on nonlinear plate aeroelastic response. 43rd AIAA/ASME/ASCE/AHS/ASCE Structures, Structural Dynamics and Materials Conference, Paper No. AIAA 2002-1271.

Mallat, S., 1999. A Wavelet Tour of Signal Processing, second ed. Academic Press, New York.

Manohar, C.S., Ibrahim, R.A., 1999. Progress in structural dynamics with stochastic parameter variations: 1987–1998. Applied Mechanics Reviews 52, 177–197.

Mastroddi, F., Bettoli, A., 1999. Wavelet analysis for Hopf bifurcations with aeroelastic applications. Journal of Sound and Vibration 225, 887–913.

Newland, D.E., 1999a. Ridge and phase identification in the frequency analysis of transient signals by harmonic wavelets. ASME Journal of Vibration and Acoustics 121, 149–155.

Newland, D.E., 1999b. Harmonic wavelets in vibrations and acoustics. Royal Society Meeting, Wavelets: The Key to Intermittent Information, February 24–25, 1999.

Potter, S., Lind, R., 2001. Developing uncertainty models for robust flutter analysis using ground vibration test data, AIAA 2001-1585, also as NASA/TM-2001-210392.

Pourtakdoust, S.H., Fazelzadeh, S.A., 2003. Chaotic analysis of nonlinear viscoelastic panel flutter in supersonic flow. Nonlinear Dynamics 32, 387–404.

Prazenica, R.J., Lind, R., Kurdila, A.J., 2003. Uncertainty estimation from Volterra kernels for robust flutter analysis. Journal of Guidance, Control, and Dynamics 26, 331–339.

Qiao, S., Pilipchuk, V.N., Ibrahim, R.A., 2000. Modeling and simulation of elastic structures with parameter uncertainties and relaxation of joints. ASME Journal of Vibration and Acoustics 123, 45–52.

Staszewski, W.J., Cooper, J.E., 2002. Wavelet approach to flutter data analysis. Journal of Aircraft 39, 125–132.

Wolf, A., Swift, J.B., Swinney, H., Vastano, J.A., 1985. Determining Lyapunov exponents from time series. Physica 16D, 285–317.

Yu, K., Ye, J., Zou, J., Yang, B., Yang, H., 2004. Missile flutter experiment and data analysis using wavelet transform. Journal of Sound and Vibration 269, 899–912.